climate

MDPI

Article

Identifying Flood Source Areas and Analyzing High-Flow Extremes Under Changing Land Use, Land Cover, and Climate in the Gumara Watershed, Upper Blue Nile Basin, Ethiopia

Haile Belay [1,2,*], Assefa M. Melesse [3,*], Getachew Tegegne [3,4] and Habtamu Tamiru [5]

[1] Africa Center of Excellence for Water Management, Addis Ababa University, Addis Ababa 1176, Ethiopia
[2] Department of Hydraulic and Water Resources Engineering, Dilla University, Dilla 419, Ethiopia
[3] Department of Earth and Environment, Florida International University, Miami, FL 33199, USA; getachewtegegne21@gmail.com
[4] Department of Civil Engineering, Sustainable Energy Center of Excellence, Addis Ababa Science and Technology University, Addis Ababa 16417, Ethiopia
[5] Department of Civil and Environmental Engineering, University of Houston, Houston, TX 77204, USA; htamirud@cougarnet.uh.edu
* Correspondence: haile.belay@aau.edu.et (H.B.); melessea@fiu.edu (A.M.M.)

Abstract: Changes in land use and land cover (LULC) and climate increasingly influence flood occurrences in the Gumara watershed, located in the Upper Blue Nile (UBN) basin of Ethiopia. This study assesses how these factors impact return period-based peak floods, flood source areas, and future high-flow extremes. Merged rainfall data (1981–2019) and ensemble means of four CMIP5 and four CMIP6 models were used for historical (1981–2005), near-future (2031–2055), and far-future (2056–2080) periods under representative concentration pathways (RCP4.5 and RCP8.5) and shared socioeconomic pathways (SSP2-4.5 and SSP5-8.5). Historical LULC data for the years 1985, 2000, 2010, and 2019 and projected LULC data under business-as-usual (BAU) and governance (GOV) scenarios for the years 2035 and 2065 were used along with rainfall data to analyze flood peaks. Flood simulation was performed using a calibrated Hydrologic Engineering Center–Hydrologic Modeling System (HEC-HMS) model. The unit flood response (UFR) approach ranked eight subwatersheds (W1–W8) by their contribution to peak flood magnitude at the main outlet, while flow duration curves (FDCs) of annual maximum (AM) flow series were used to analyze changes in high-flow extremes. For the observation period, maximum peak flood values of 211.7, 278.5, 359.5, 416.7, and 452.7 m^3/s were estimated for 5-, 10-, 25-, 50-, and 100-year return periods, respectively, under the 2019 LULC condition. During this period, subwatersheds W4 and W6 were identified as major flood contributors with high flood index values. These findings highlight the need to prioritize these subwatersheds for targeted interventions to mitigate downstream flooding. In the future period, the highest flow is expected under the SSP5-8.5 (2056–2080) climate scenario combined with the BAU-2065 land use scenario. These findings underscore the importance of strategic land management and climate adaptation measures to reduce future flood risks. The methodology developed in this study, particularly the application of RF-MERGE data in flood studies, offers valuable insights into the existing knowledge base on flood modeling.

Keywords: climate change; land use and land cover change; flood source area identification; Gumara watershed; HEC-HMS; high-flow extremes

check for updates

Academic Editors: Yang Zhou and Jiabao Wang

Received: 11 November 2024
Revised: 16 December 2024
Accepted: 30 December 2024
Published: 1 January 2025

Citation: Belay, H.; Melesse, A.M.; Tegegne, G.; Tamiru, H. Identifying Flood Source Areas and Analyzing High-Flow Extremes Under Changing Land Use, Land Cover, and Climate in the Gumara Watershed, Upper Blue Nile Basin, Ethiopia. *Climate* **2025**, *13*, 7. https://doi.org/10.3390/cli13010007

Copyright: © 2025 by the authors. Licensee MDPI, Basel, Switzerland. This article is an open access article distributed under the terms and conditions of the Creative Commons Attribution (CC BY) license (https://creativecommons.org/licenses/by/4.0/).

1. Introduction

Recently, flooding has become the most common and leading environmental hazard, with diverse impacts on human life, property, socioeconomic development, and agricultural production [1,2]. It is aggravated mostly by factors such as land use and land cover (LULC) and climate changes [3,4]. LULC changes such as deforestation, agricultural expansion, and urbanization result in an increase in surface runoff by changes in the hydrologic characteristics of basins and watersheds [5,6], while climate change causes flooding by changing the frequency, magnitude, and duration of extreme rainfall events [7–9].

For projecting extreme rainfall events that would cause flooding, general circulation models (GCMs) available in the Coupled Model Intercomparison Project Phases 5 and 6 (CMIP5 and CMIP6) play a significant role [10,11]. However, these models are often associated with biases due to their coarse spatial resolution [12]. To address this issue, the use of high-resolution downscaled outputs, such as those from the NASA Earth Exchange-Global Daily Downscaled Projections (NEX-GDDP) dataset, is generally recommended [13,14]. The NASA NEX-GDDP-CMIP5 and CMIP6 datasets provide daily temporal resolution and a spatial resolution of 0.25° (approximately 25 km × 25 km), making them suitable for watershed- and basin-scale studies [15,16]. Furthermore, the biases associated with climate models can be mitigated by evaluating and selecting the best-performing models, applying bias correction techniques, and using multi-model ensemble means of bias-corrected models [17–19].

Historical LULC maps generated from remotely sensed images have been extensively used to assess past watershed and basin conditions [3,20–22]. Additionally, projected LULC maps under different scenarios are crucial for understanding future conditions. Consequently, several studies have focused on LULC predictions in different regions [23–25]. For example, in the Gumara watershed, Belay et al. [26] projected future LULC changes under a business-as-usual (BAU) scenario and a governance (GOV) scenario. The BAU scenario assumes the continuation of current trends in land use change and socioeconomic development, whereas the GOV scenario incorporates the Green Legacy Initiative (GLI), a program currently being implemented by the Ethiopian government. Their study revealed significant expansion in cultivated land and settlements under the BAU scenario, whereas the GOV scenario predicted increases in forest, shrubland, and grassland. Similarly, a study by Gebresellase et al. [27] in the upper Awash basin of Ethiopia reported the expansion of agricultural lands and urban settlements under the BAU scenario and improvements in forest cover under the GOV scenario.

Flood occurrence can be studied by estimating peak floods for different return periods. This is a crucial aspect in designing safe and cost-effective flood protection structures to minimize the destructive impacts of flooding on the environment [28–30]. Return period-based peak floods can be estimated using statistical flood frequency analysis and hydrological rainfall–runoff models. The traditional statistical flood frequency analysis involves estimation of flood quantiles via a best-fitting probability distribution on the basis of the assumption that historical discharge time series are stationary and independent [31]. However, rainfall–runoff hydrological models simulate the transformation of design storms (rainfall) into design floods, taking into account the effects of changing LULC and climate [32–34].

Flooding mostly occurs at certain downstream reaches of the main river. Hence, before flood control structures are constructed, quantifying the contribution of upstream subwatersheds to the peak flood magnitude at the main outlet of the watershed is often recommended. This method is commonly known as flood source area identification (FSAI) [35]. FSAI can be performed via multicriteria evaluation (MCE) and the unit flood response (UFR) approach [36]. The MCE approach can be implemented via a geographic information

system (GIS), which considers the linear combination of the weights of several flood control factors [37,38]. However, this approach does not account for flow routing through rivers. The second approach, UFR, can be performed via hydrological models by accounting for flood routing through rivers for watersheds with diverse conditions [36]. This method was first applied to the Damavand watershed in Iran by Saghafian and Khosroshahi [35] and has since been used in various watersheds. For example, Abdulkareem et al. [39] employed the UFR approach to assess the impact of LULC changes on FSAI for the Kelantan basin in Malaysia. In their study, the authors employed the Hydrologic Engineering Center–Hydrologic Modeling System (HEC-HMS) model and stated its importance for ranking subwatershed units on the basis of their contribution to peak discharge at the main outlet. Similarly, Fiorillo and Tarchiani [40] applied this approach to a catchment in Niger and reported its suitability for identifying flood source areas.

Several studies conducted across various basins and watersheds have demonstrated a potential increase in high-flow extremes in future periods. These studies typically employed hydrological models to simulate future streamflow based on GCM outputs. For instance, Yang et al. [41] assessed future changes in high-flow extremes in the Jiulong River Basin of Southeast China by simulating streamflow under changing LULC and climate conditions. Their findings indicated an increase in high-flow extremes due to intensified extreme rainfall and LULC changes driven by human activities. Similarly, Mahato et al. [42] showed an increase in flood frequency in the Brahmani River basin, India, by simulating streamflow using a semi-distributed hydrological model driven by outputs from CMIP6 models. In the Ethiopian context, Kassaye et al. [43] showed a projected increase in high-flow extremes in the Baro River Basin by simulating streamflow using six GCMs under different scenarios. Likewise, Yalcin [44] indicated a projected rise in flood frequency in Bitlis Creek, Turkey.

The downstream area of the Gumara watershed, particularly near Lake Tana, is one of the most flood-affected regions in the Upper Blue Nile (UBN) basin of Ethiopia [45]. Several studies have addressed flood risk in this area through different approaches, including flood hazard mapping using the MCE method [46], statistical flood frequency analysis [30], hydraulic flood inundation modeling [47], and flood mapping via Sentinel-1 images [48]. However, return period-based peak flood estimation, FSAI, and extreme flow estimations under varying LULC and climate scenarios remain underexplored in the upstream region of the watershed. Additionally, most flood simulation studies in the Gumara watershed have relied on ground-based rainfall data. However, these observations often contain uncertainties due to missing data, sparse rain gauge networks, and the influence of topography [49,50]. To overcome these limitations, recent studies [51–53] have suggested merging ground-based rainfall data with gridded rainfall products (GRFPs). This approach enhances the accuracy of flood simulations by reducing the uncertainties of ground-based rainfall measurements.

Hence, the objectives of this study are to (1) examine the impact of LULC change on return period-based peak floods and flood source areas (FSA) for the observation period (1981–2019) and (2) assess the combined impacts of LULC and climate change on high-flow extremes, considering historical (1981–2005), near-future (2031–2055), and far-future (2056–2080) periods. To achieve these objectives, flood simulations were performed using a calibrated and validated HEC-HMS model.

For the observation period, the study utilized merged rainfall estimates from ground-based observed rainfall and three gridded rainfall products (GRFPs): Multi-Source Weighted-Ensemble Precipitation (MSWEP) [54], Climate Hazards Group InfraRed Precipitation with Stations (CHIRPS) [55], and the Enhanced Global Dataset for the Land Component of the Fifth Generation of European Reanalysis (ERA5-Land) [56]. The merging process was performed using a random forest merging algorithm (RF-MERGE). LULC

maps for the years 1985, 2000, 2010, and 2019 were incorporated alongside these merged rainfall estimates for this period.

To assess changes in high-flow extremes between historical and future periods under changing LULC and climate conditions, high flow simulations were conducted using bias-corrected ensemble means of historical and projected rainfall data from four CMIP5 and four CMIP6 models. For the projected rainfall, the study accounted for representative concentration pathways (RCP4.5 and RCP8.5) for CMIP5 models and shared socioeconomic pathways (SSP2-4.5 and SSP5-8.5) for CMIP6 models. Additionally, future LULC scenarios under the BAU and GOV scenarios for 2035 and 2065 were considered for the near-future and far-future periods, respectively, alongside the future climate scenarios.

In summary, this study offers valuable insights into prioritizing flood source areas in the Gumara watershed and proposes targeted runoff reduction mechanisms. The estimation of high-flow extremes provides critical input for developing effective flood risk protection strategies, while the study's methodology serves as a framework for flood simulations in similar watersheds across the UBN basin and beyond.

2. Materials and Methods

2.1. Study Area

The Gumara watershed is part of the Lake Tana subbasin, which is located in the UBN basin of Ethiopia (Figure 1). The watershed is primarily drained by the Gumara River, which originates from Guna Mountain. Geographically, it spans from 11°35′ N to 11°55′ N latitude and from 37°35′ E to 38°15′ E longitude. The drainage area of the watershed is approximately 1256.7 km^2. The topography of the watershed is diverse, with elevations ranging from 1792 to 3708 m above mean sea level (amsl) (Figure 1c). It is characterized by steep gradients and mountainous terrain in its upstream areas and flat downstream floodplains. The watershed experiences a unimodal rainfall pattern, with the main rainy season occurring from June to September. The watershed receives an average annual rainfall of 1445 mm, and its average annual temperature is about 20.5 °C [57]. LULC in the watershed is dominated by cultivated land, which accounts for more than 80% of the total area, while the remaining portion of the watershed comprises forest, shrubland, grassland, and settlement areas [26]. The predominant soil texture classes in the region include clay, clay loam, sandy clay, silty clay, and silty clay loam [48]. The majority of the watershed is characterized by scattered rural settlements, where the local livelihood is primarily based on a mixed farming system (crop cultivation and livestock raising) [58]. The downstream part of the watershed, which is adjacent to Lake Tana, is susceptible to frequent flood events due to high runoff generated from the upland watershed [46,59].

2.2. Data Used

For this study, various spatial and temporal data were collected from different sources. These include observed ground-based rainfall and streamflow, gridded rainfall products, climate model data, and spatial data such as elevation, soil, and LULC data.

2.2.1. Observed Ground-Based Rainfall and Streamflow Data

Ground-based daily rainfall data from eight meteorological stations located in and around the Gumara watershed were collected from the National Meteorological Agency (NMA) of Ethiopia, covering the long-term observation period from 1981 to 2019 (Table 1).

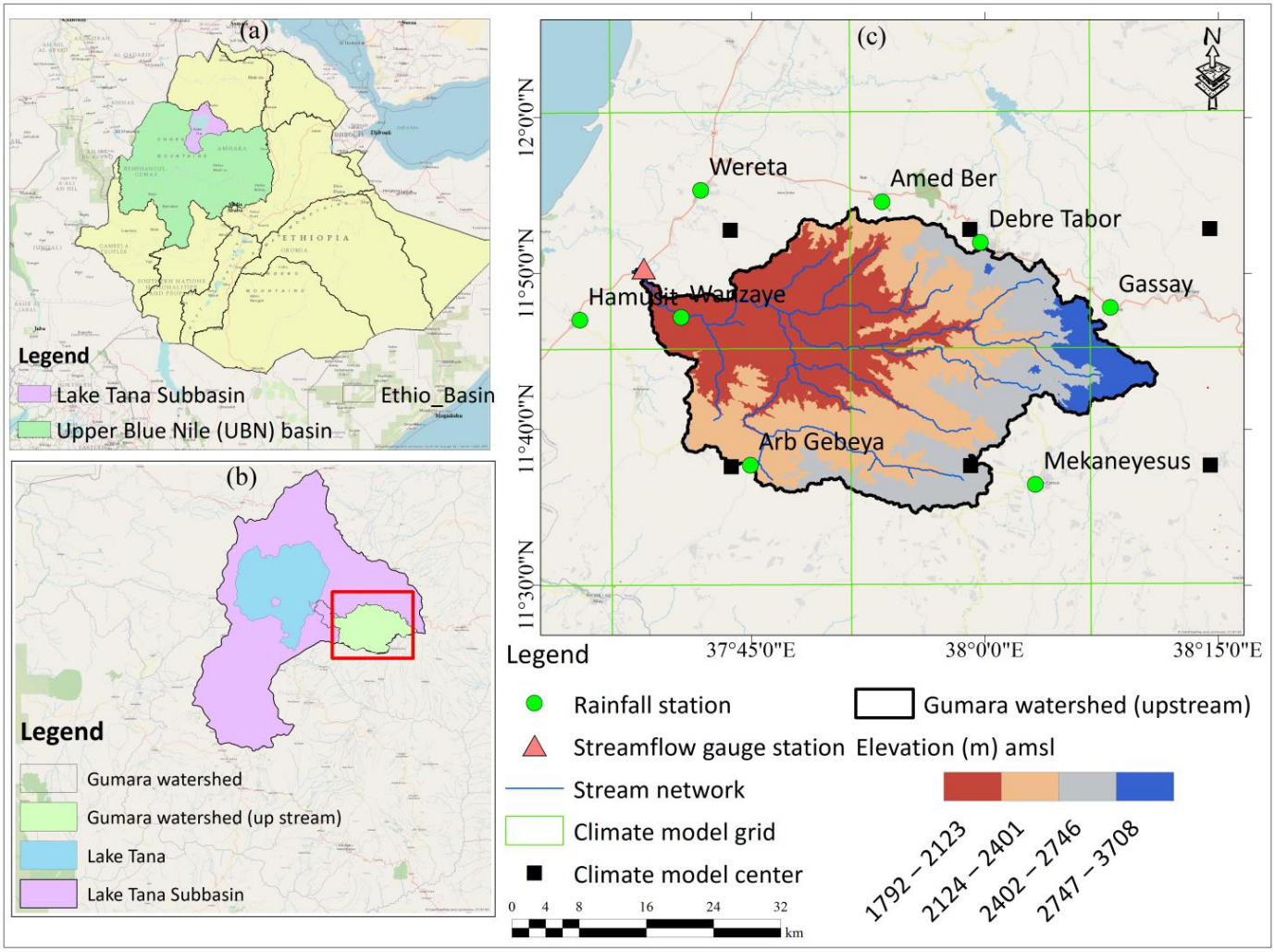

Figure 1. Location map of the study area. (**a**) Location map of the Upper Blue Nile (UBN) basin within the 12 river basins of Ethiopia. (**b**) Location map of the upstream Gumara watershed (bounded by a red rectangle) within the Lake Tana subbasin, and (**c**) Detailed map showing the rainfall and streamflow gauging stations, stream network, climate model grid (25 km × 25 km), and grid center for the NASA dataset, and elevation map of the upstream (flood source area) part of the Gumara watershed.

Table 1. Location and elevation information of the eight ground-based meteorological stations located in and around the Gumara watershed.

No.	Station Name	Latitude (°)	Longitude (°)	Elevation (m)
1	Amed Ber	11.91	37.88	2051
2	Arb Gebeya	11.62	37.74	2248
3	Debre Tabor	11.87	38.01	2612
4	Gassay	11.79	38.13	2789
5	Hamusit	11.78	37.56	1954
6	Mekaneyesus	11.58	37.90	2374
7	Wanzaye	11.78	37.68	1821
8	Wereta	11.92	37.70	1819

The observed daily streamflow time series data (1981–2019) for the Gumara River at the Wanzaye gauging station were obtained from the Ministry of Water, Irrigation, and Electricity (MoIR) of Ethiopia. Selected events from this dataset were utilized for hydrological model sensitivity analysis, calibration, and validation.

2.2.2. Gridded Rainfall Products (GRFPs)

In watersheds with diverse topographies, such as the Gumara watershed, sparsely distributed meteorological stations may not adequately capture rainfall characteristics. To address this issue, three GRFPs were accessed and merged with ground-based observed rainfall. The three GRFPs selected for this study were MSWEP, CHIRPS, and ERA5-Land. MSWEP is a global gridded rainfall product that integrates multiple data sources, including satellite observations, gauge data, and reanalysis products, with a spatial resolution of 0.1° × 0.1° (approximately 10 km × 10 km). CHIRPS combines satellite-based infrared imagery with ground station data to provide a high-resolution rainfall product with a spatial resolution of 0.05° × 0.05° (approximately 5 km × 5 km). ERA5-Land provides high-resolution reanalysis rainfall data produced by the European Centre for Medium-Range Weather Forecasts (ECMWF), with a spatial resolution of 0.1° × 0.1° (approximately 10 km × 10 km). These GRFPs were selected due to their superior performance in reproducing the rainfall characteristics of the UBN basin [60,61]. For this study, CHIRPS and ERA5-Land at each ground-based station were accessed via the Climate Engine (https://www.climateengine.org/), while the MSWEP dataset was extracted using a Python environment. For the three GRFPs, the time series data were accessed at a daily temporal scale for a common period (1981–2019). Table 2 summarizes the spatial resolutions, access, and references for these datasets.

Table 2. Details of the gridded rainfall products (GRFPs) used in the rainfall data merging process.

Gridded Rainfall Product	Spatial Resolution (km)	Source URL (Accessed Date Day/Month/Year)	Reference
MSWEP	10 km × 10 km	https://www.gloh2o.org/mswep (accessed on 1 February 2024)	[54]
CHIRPS	5 km × 5 km	https://www.chc.ucsb.edu/data/chirps/ (accessed on 15 February 2024)	[55]
ERA5-Land	10 km × 10 km	https://www.ecmwf.int/en/era5-land (accessed on 25 February 2024)	[56]

2.2.3. General Circulation Models (GCMs)

Historical (1981–2005), near-future (2031–2055), and far-future (2056–2080) rainfall data from four selected CMIP5 and four CMIP6 models were accessed from the NASA NEX-GDDP dataset. The time series rainfall data for these models were extracted for each ground-based meteorological station using a Google Earth Engine (GEE) sample script, available at this repository: https://code.earthengine.google.com/74643b20363d1f0d4ee5875c456f5c14. For the CMIP5 models, future scenarios considered were RCP4.5 and RCP8.5, while for the CMIP6 models, SSP2-4.5 and SSP5-8.5 were utilized. The models were chosen on the basis of their better performance in reproducing historical extreme rainfall in the UBN basin following our recent work [62]. All the CMIP5 and CMIP6 models are statistically downscaled outputs with a daily temporal resolution and 25 km × 25 km spatial resolution. Table 3 summarizes detailed descriptions, including the resolutions of the climate models, modeling centers, and countries of the selected climate models. Details on the comparison and evaluation of the performance of the CMIP5 and CMIP6 models can be found in Belay et al. [62].

Table 3. Descriptions of the NASA NEX-GDDP dataset (CMIP5 and CMIP6 climate models) used in this study.

GCM	Name	Spatial Resolution (km)	Modeling Center	Country
CMIP5	MIROC5	25 km × 25 km	National Institute for Environmental Studies, the University of Tokyo	Japan
	MRI-CGCM3	25 km × 25 km	Meteorological Research Institute	Japan
	CanESM2	25 km × 25 km	Canadian Centre for Climate Modeling and Analysis	Canada
	MPI-ESM1-2-LR	25 km × 25 km	Max Planck Institute for Meteorology	Germany
CMIP6	MPI-ESM1-2-LR	25 km × 25 km	Max Planck Institute for Meteorology	Germany
	MRI-ESM2-0	25 km × 25 km	Meteorological Research Institute	Japan
	CNRM-CM6-1	25 km × 25 km	Centre National de Recherches Meteorologiques	France
	BCC-CSM2-MR	25 km × 25 km	Beijing Climate Center, China Meteorological Administration	China

2.2.4. Elevation, Soil, and LULC Data

The elevation data of the study watershed were extracted from a 30 m spatial resolution digital elevation model (DEM) of the Shuttle Radar Topography Mission (SRTM) [63]. The SRTM DEM data was accessed from USGS Earth Explorer via this link: https://earthexplorer.usgs.gov/. The data was primarily used to generate subwatershed units and other watershed characteristics, including watershed slope and stream network.

Hydrologic Soil Groups (HSGs) for the study area were extracted from a 250 m spatial-resolution soil grid map established by the USDA. The data was accessed via this link: https://daac.ornl.gov/cgi-bin/dsviewer.pl?ds_id=1566. As shown in Figure 2c, HSG-D (clay loam, sandy clay, silty clay, silty clay loam, or clay) covers approximately 89% of the study watershed. These soils have high runoff potential because of very slow infiltration rates [64]. The remaining portion of the study watershed is covered by HSG-C (sandy clay loam). These soils have a moderately high runoff potential due to slow infiltration rates [64].

Raster files of historical and future LULC maps of the Gumara watershed, with a 30 m spatial resolution, were clipped from our previous work [26], which accounted for the entire Gumara watershed. In that work [26], the LULC maps were generated using composite images from Landsat-5/Thematic Mapper (TM) for the years 1985, 2000, and 2010, and Landsat-8/Operational Land Imager (OLI) for the year 2019. For these years, cloud-free images from January to March were accessed from the U.S. Geological Survey via the GEE data catalog. LULC classification was performed using a random forest (RF) algorithm [65] in the GEE environment, resulting in the identification of five dominant classes: forest, shrubland, grassland, cultivated land, and settlement areas, which describe the land use conditions of the study watershed. Specific information on the Landsat mission used, acquisition dates, and path/row details can be in the Supplementary Materials (Table S1).

In our previous work [26], future land use prediction was performed via the Cellular Automata-Markov (CA-Markov) model available in the land change modeler (LCM) module of IDRISI Selva 17.0 [66]. For the prediction, historical LULC maps (baseline) and various land-use change driver variables were considered, including elevation, slope, distance from roads, distance from streams, distance from towns, and socio-economic development (evidence of the likelihood of change). The prediction was conducted under two "what-if" scenarios: the business-as-usual (BAU) scenario and the governance (GOV) scenario. The BAU scenario considered the current trend of land use conversion and change drivers (transition probability), whereas the GOV scenario accounted for the massive tree

seedling plantation program of the Ethiopian government, known as the Green Legacy Initiative (GLI) program [67]. Figure 2d–k show historical and predicted LULC maps of the Gumara watershed. Details on methods used for classification, accuracy assessment, LULC change drivers, scenario-based LULC prediction, and change detection for the entire Gumara watershed can be found in Belay et al. [26].

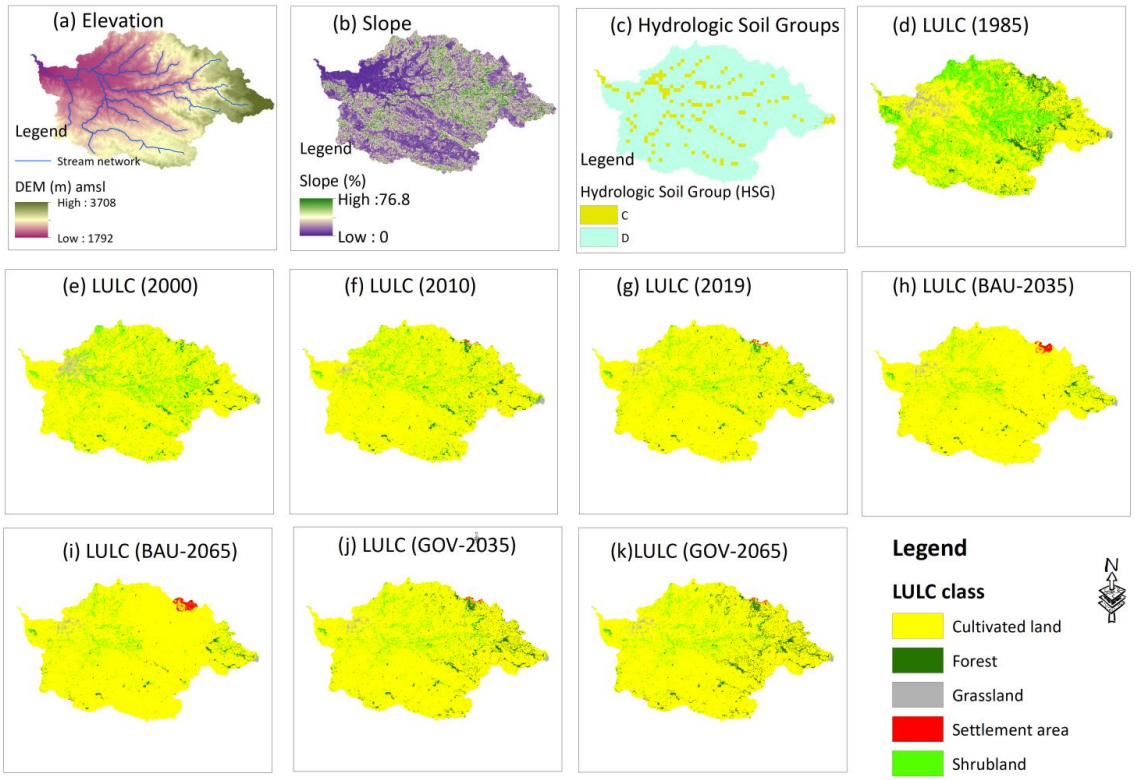

Figure 2. (**a**) Elevation, (**b**) slope, (**c**) hydrologic soil groups (HSGs), and (**d**–**k**) historical and projected land use and land cover maps of the Gumara watershed for the historical (1985, 2000, 2010, and 2019) and future years (2035 and 2065) under the business-as-usual (BAU) and governance (GOV) scenarios.

2.3. Methods

This study analyzed peak floods for different return periods (5-, 10-, 25-, 50-, and 100-year) and flood source areas during the observation period (1981–2019) under varying LULC conditions. Additionally, high-flow extremes were assessed for historical (1981–2005) and future (2031–2080) periods under different LULC and climate scenarios. The analysis involved collecting and processing spatiotemporal data, including daily ground-based rainfall, streamflow, GRFPs (MSWEP, CHIRPS, and ERA5-Land), CMIP5 and CMIP6 models, elevation, LULC, and soil data.

Ground-based rainfall data were merged with the three GRFPs using the RF-MERGE algorithm [65] to enhance data accuracy. The merging process included four main steps: input data preparation, setting up the RF model, training the RF model, and performing the merging (prediction). For merging, ground-based rainfall data were used as the dependent variable, while GRFPs and other auxiliary data were used as independent variables. The resulting merged rainfall product was subsequently utilized in rainfall–runoff modeling for extracting annual maximum (AM) 1-day rainfall series, and for correcting biases in climate model outputs. In the study, rainfall data from CMIP5 (MIROC5, MRI-CGCM3, CanESM2, and MPI-ESM1-2-LR) and CMIP6 (MPI-ESM1-2-LR, MRI-ESM2-0, CNRM-CM6-1, and BCC-CSM2-MR) models were also bias corrected, and their ensemble means were predicted for historical and future periods to reduce uncertainties associated with climate models. Bias correction was performed using the quantile mapping (QM) method [68]. From the

corrected daily rainfall data, AM 1-day rainfall series were extracted and subsequently used to estimate high-flow extremes in the near-future and far-future periods.

Flood simulation was conducted using the HEC-HMS model (version 4.11) [69]. The process included subwatershed delineation, entering rainfall data, model selection, parameter estimation and sensitivity analysis, calibration and validation, and flood simulation under various climate and LULC scenarios. Using the calibrated model, peak floods for different return periods were determined, flood source areas prioritized, and high-flow extremes for historical and future periods assessed. The overall methodology is outlined in Figure 3, with detailed explanations in subsequent sections.

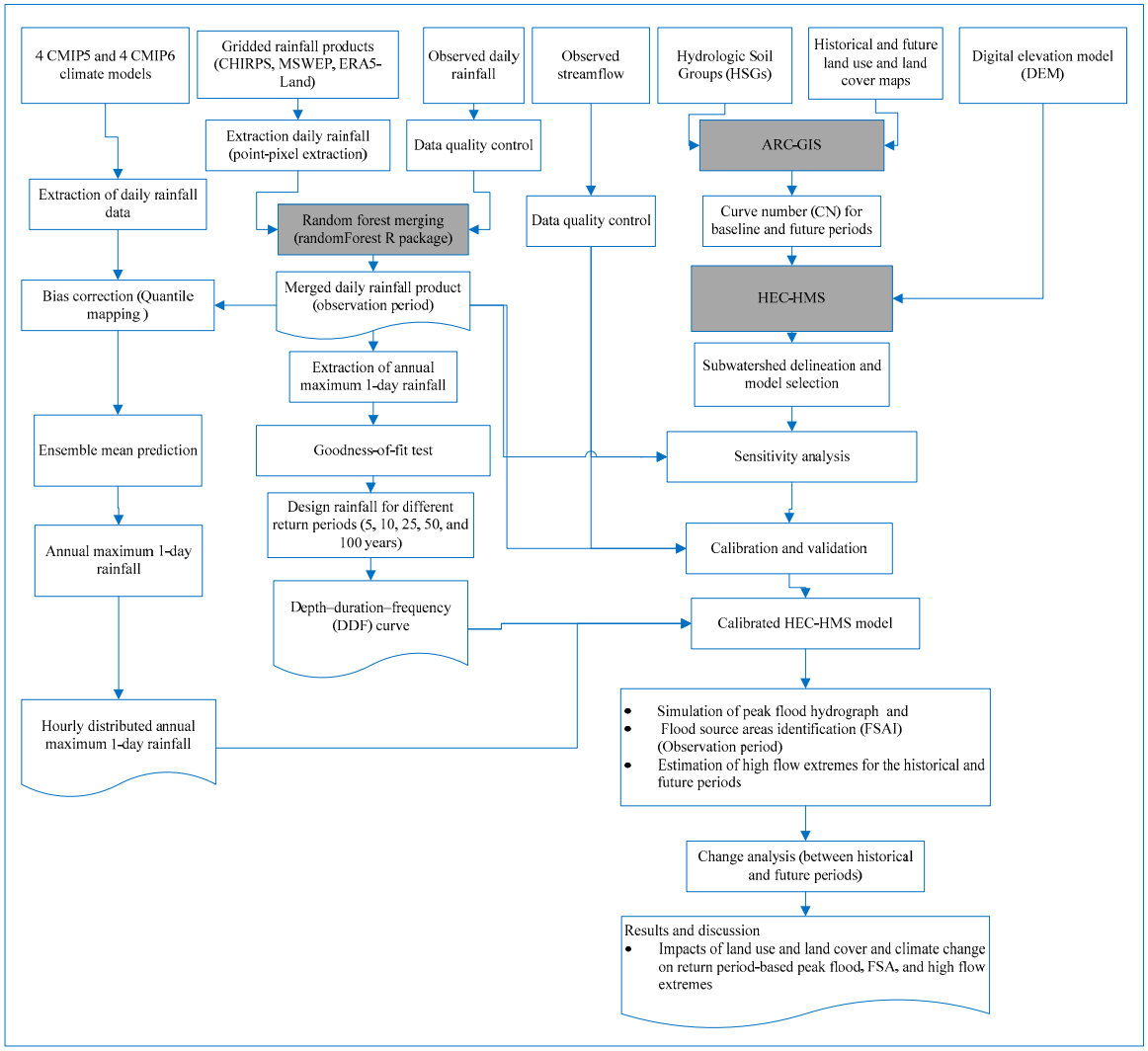

Figure 3. Methodological framework of the study. In the figure, boxes highlighted with grey color represent the main processing algorithm, tool, and hydrological model used in the study.

2.4. Data Quality Control

In hydroclimatic studies, the use of long-term, homogeneous, and consistent data is generally recommended. However, the ground-based stations considered in this study have missing rainfall data and short-term rainfall records at the Hamusit, Wanzaye, and Arb Gebeya stations. The missing data were filled via the inverse distance weighting (IDW) technique, whereas short-term rainfall records were extended via the maintenance of variance extension, type 1 (MOVE.1) technique [70]. After filling in missing data and extending short-term data, a homogeneity test was employed to detect change points in the mean annual rainfall data via the nonparametric Pettitt test [71]. According to the Pettitt

test statistics presented in the Supplementary Materials (Table S2), no significant changes were detected in the annual rainfall data for the stations considered in this study.

Double-mass curve (DMC) analysis was also employed to check the consistency of the mean annual rainfall data. This analysis involved inspecting significant changes in slope by plotting the cumulative mean annual rainfall of all stations on the *x*-axis and the cumulative mean annual rainfall of each station on the *y*-axis. From the analysis, all the stations were found to be consistent (Figure 4a), since no significant changes in slope were detected in the DMC plot. Figure 4b–d also present mean annual rainfall at each ground-based station, mean monthly rainfall, and mean monthly discharge data, respectively.

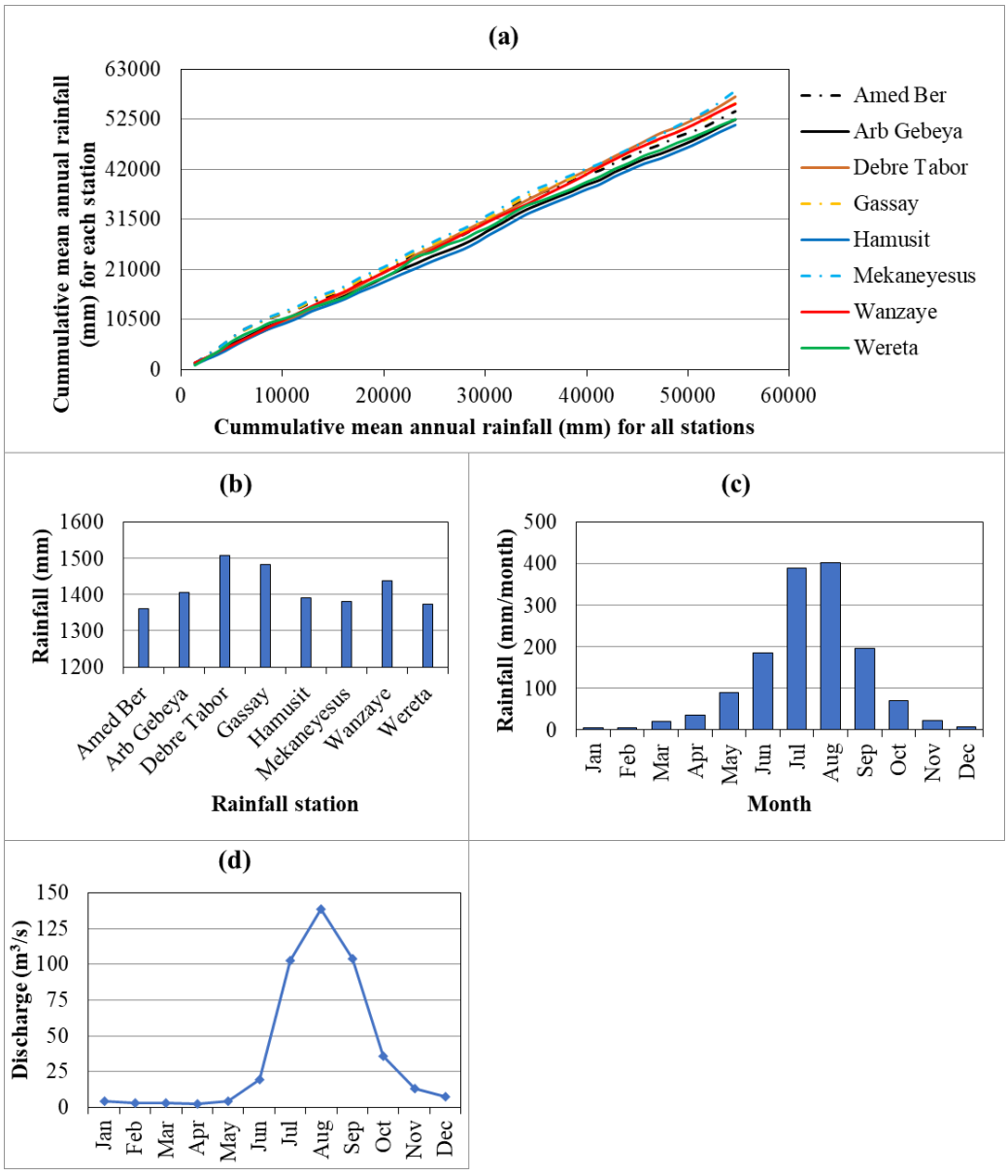

Figure 4. Observed ground-based rainfall and discharge data from 1981 to 2019 for the Gumara watershed. (**a**) Double mass curve analysis, (**b**) mean annual rainfall of each ground-based rainfall station, (**c**) mean monthly rainfall, and (**d**) mean monthly discharge.

2.5. Random Forest Merging (RF-MERGE)

To improve the quality of the rainfall data, the random forest (RF) merging approach (RF-MERGE) was employed to combine daily ground-based observed rainfall with three GRFPs (MSWEP, CHIRPS, and ERA5-Land). RF is a supervised machine learn-

ing algorithm that can be used for both classification and regression [65]. Among the various merging approaches, RF-MERGE was selected based on our previous work [62], conducted in the study region. In that study, RF-MERGE demonstrated the best performance in reproducing observed rainfall compared to individual GRFPs and other merging approaches, as evaluated by both statistical and categorical performance measures. Additionally, RF-MERGE requires a minimal number of model parameters and is capable of handling high-dimensional data [52].

For the merging process, ground-based rainfall data, three GRFPs, and auxiliary data (including date, month, year, and elevation) were first prepared. Next, the RF model was set up to map the relationship between the dependent and independent variables. In this study, ground-based rainfall data served as the dependent variable, while the three GRFPs, along with the auxiliary data, were used as independent variables. Subsequently, the RF algorithm was trained using rainfall data recorded at stations located in the UBN basin (Table S3 in the Supplementary Materials). During training, the RF model learned the relationship between the dependent and independent variables. Based on this, the optimal parameter values of the RF algorithm, such as the number of trees (N_t), the minimum number of bootstrap samples (N_{min}), and the number of features (N_f) at the splitting node, were estimated. Finally, using the trained RF model, rainfall was predicted at stations located in and around the Gumara watershed (Table 2). The merging procedure was performed via the "randomForest" R package version 4.7 [72]. The analysis yielded estimated parameter values of 200, 6, and 3 for N_t, N_{min}, and Nf, respectively. These parameters were determined through trial-and-error procedures and by comparison with parameters estimated in previous studies [73,74]. Using these parameters, the trained model was subsequently used to predict daily rainfall at the eight testing stations. The merged rainfall data were then used to extract the AM 1-day rainfall, correct the bias of the climate models, and calibrate/validate the hydrological model. A comprehensive review, including assumptions, procedures, and limitations of various merging approaches, such as RF-MERGE, can be found in our previous work [50].

2.6. Design Rainfall and Depth–Duration–Frequency (DDF) Curve

In this study, the annual maximum 1-day rainfall data series for the observation period (1981–2019) was extracted and fitted to commonly used probability distributions: normal (NOR), lognormal (LN3), gamma (GAM), Gumbel (GUM), Pearson type III (PE3), log Pearson type III (LPE3), and generalized extreme value (GEV) distributions. The parameters of these distributions were calculated via the L-moments method provided in Hosking and Wallis [31]. The Anderson–Darling (AD) test [75] was employed to assess goodness of fit by comparing the CDFs of the observed data with those of the candidate distributions. This test is sensitive to deviations in the tails of the probability distribution, making it valuable for applications involving extreme values [76]. The best-fit distribution was selected on the basis of the lowest AD statistic (A^2) at the 5% significance level and used for estimating design rainfall for different return periods.

To simulate flood hydrographs for different return periods (5-, 10-, 25-, 50- and 100-year), a short-duration (example with an hourly distribution) depth–duration–frequency (DDF) curve is often needed. For this, a short-duration hourly distributed DDF curve was developed using the following equation:

$$R_t = R_{24}\left(\frac{t}{24}\right)\left(\frac{b+24}{b+t}\right)^n \quad (1)$$

where R_t is the computed rainfall depth for a duration of t hours, R_{24} is the design rainfall depth for a 24-h (1-day) duration, t is the rainfall duration in hours, b is a parameter that

controls the relationship between different durations and can be determined on the basis of regional studies, and n is an exponent that adjusts the amount at which rainfall decreases with shorter durations and can be determined empirically on the basis of regional studies. For this study, the DDF curve for a 1-h duration was developed using 0.3 for the parameter b and 0.9 for the exponent n following regional studies conducted in Ethiopia [77,78].

2.7. Bias Correction

It is common for climate model simulations to exhibit bias (uncertainties) due to their coarse spatial resolution, model assumptions, boundary conditions, spatial averaging, and other factors [79,80]. To address this issue, it is generally recommended that biases in climate models be corrected before their outputs are applied in impact assessment studies [81]. Among the different types of bias correction methods, the QM approach was used in this study because of its better performance in the study region [62]. The QM method uses the quantile–quantile relationship to match the distribution function of climate model simulations with observed data [68]. The method assumes that the cumulative distribution functions (CDFs) of the observed and simulated datasets can be matched, meaning that the CDFs of the observed and simulated data should be similar enough for meaningful bias correction [82]. Based on this assumption, for a given simulated value x_{sim}, QM bias correction adjusts it using:

$$x_{cor} = F_{obs}^{-1}[F_{sim}(x_{sim})] \quad (2)$$

where x_{cor} is bias corrected value, $F_{sim}(x_{sim})$ is CDF of the simulated data, $F_{obs}(x)$ is CDF of the observed data, and F_{obs}^{-1} is inverse CDF (quantile function) of the observed data.

In this study, prior to implementing QM bias correction, the CDFs of daily observed rainfall from RF-MERGE and simulated rainfall from historical CMIP5 and CMIP6 were computed and plotted, as shown in Figure 5, to assess their similarity. The graph indicates that the CDFs of the observed and simulated data are sufficiently similar, allowing the QM method to be applied.

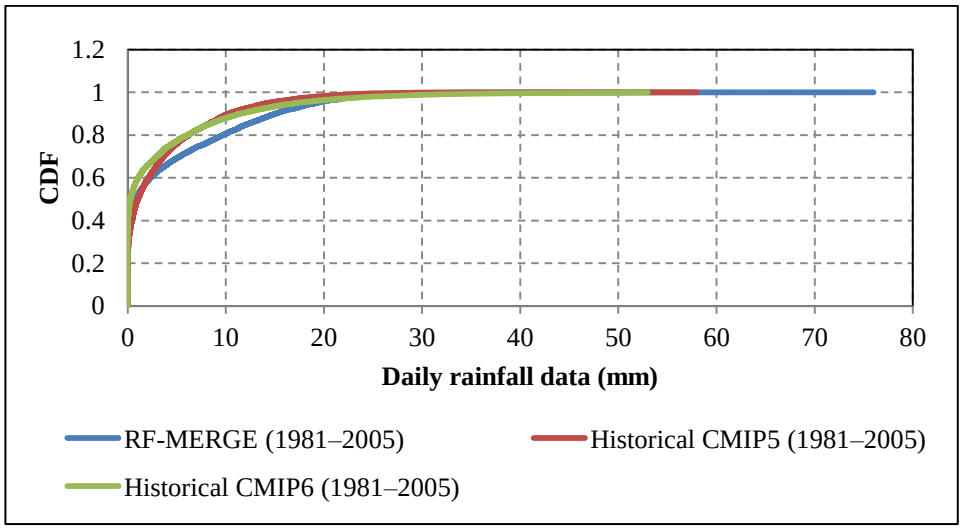

Figure 5. Comparison of cumulative distribution functions (CDFs) of daily observed rainfall data from RF-MERGE and historical CMIP5 and CMIP6 models for the period 1981–2005.

Among the different types of QM approaches, the parametric transformation function (PTF) was chosen for this study because of its effectiveness in studying extreme rainfall events [83]. The bias correction was applied by matching the historical climate model data with the RF-MERGE data and then applying the correction to the future climate model

data on the basis of historical relationships. A detailed explanation of the assumptions and formulations of the various QM bias correction methods can be found in Enayati et al. [82].

2.8. Rainfall–Runoff Modeling

Rainfall–runoff modeling can be conducted using various distributed and semi-distributed hydrological models. According to Ghonchepour et al. [84], factors such as modeling objectives, hydrologic conditions, limitations, assumptions, and data availability should guide model selection. In this study, the HEC-HMS model was chosen for its suitability in simulating rainfall–runoff processes under varying LULC and climatic conditions, aligning well with the study's objectives. HEC-HMS is a physically based, semi-distributed model widely recognized for its effectiveness in flood modeling [85–87]. It is compatible with the input data used in this study, including rainfall, streamflow, LULC, soil, and DEM data. Its semi-distributed structure facilitates accurate flow simulation at the subwatershed scale, which is critical for identifying flood source areas. Furthermore, HEC-HMS has been thoroughly tested and shown to perform well in modeling floods in similar watersheds within the UBN basin of Ethiopia [88,89].

The HEC-HMS model consists of several key components (managers), including basin models, meteorological models, time-series data, and control specifications [69]. The basin model defines the physical characteristics of the watershed, such as subwatersheds, river reaches (networks), junctions, outlets, and others, along with relevant hydrological parameters. The meteorological model specifies the type of rainfall data used in the simulation. The time-series data component is used to input rainfall and streamflow data, which are essential for driving the model. Lastly, control specification manages or sets the simulation time step, duration, and output intervals. These components work together to simulate hydrologic processes and provide flood hydrographs.

In this study, rainfall–runoff simulations in the HEC-HMS model involved subwatershed delineation (basin model), entering rainfall and streamflow data, model selection (for runoff volume, direct runoff, and routing), parameter estimation and sensitivity analysis, model calibration and validation, and flood hydrograph simulations under changing LULC and climate conditions as detailed in the subsequent sections.

2.8.1. Subwatershed Delineation

Subwatershed delineation was performed using a 30 m resolution SRTM-DEM via the GIS tools in HEC-HMS 4.11, as this version is integrated with GIS components. The process involved setting up the coordinate system (projection), terrain reconditioning, filling sinks, drainage line processing, identifying streams, defining outlets, and delineating subwatersheds. Since the middle and upper portions of the Gumara watershed lie in steep gradient areas (slope greater than 15%), the 30 m DEM resolution could introduce inaccuracies, particularly in calculating flow direction and accumulation. These limitations may result in misrepresentation of the river network of the watershed. To address this issue, DEM reconditioning techniques, such as stream burning and sink filling, were applied to improve the representation of hydrological features. Additionally, during subwatershed delineation, the homogeneity of various watershed characteristics, such as soil, LULC, elevation, and stream networks, was considered for merging similar smaller subwatersheds into one.

2.8.2. Rainfall and Streamflow Data

This study utilized daily rainfall data from RF-MERGE (1981–2019), rainfall DDF curves for return periods of 5, 10, 25, 50, and 100 years, and rainfall for both historical and future periods to simulate streamflow. Observed streamflow data for the Gumara River

(1981–2019) were also employed to compare with simulated flows during model calibration and validation, focusing on selected flood events.

2.8.3. Model Selection

In the HEC-HMS, there are various models for computing runoff volume, direct runoff, and channel flow routing. For this study, the Soil Conservation Service Curve Number (SCS-CN) [90], SCS unit hydrograph (SCS-UH) [90], and Muskingum channel routing [91] models were selected for modeling runoff volume, direct runoff, and channel flow routing, respectively.

I. Modeling runoff volumes (loss model)

Models available in the HEC-HMS generally compute runoff volume by subtracting the sum of various losses from the accumulated rainfall. Among these models, the Soil Conservation Service Curve Number (SCS-CN) method was selected for this study because it can compute runoff volume for a given rainfall event as a function of HSGs, LULC, and antecedent soil moisture conditions.

In the SCS-CN model, the excess rainfall (R_e) at a given time t is the rainfall in excess of the infiltration capacity and other losses and can be computed as:

$$R_e = \frac{(R - I_a)^2}{R - I_a + S} \quad (3)$$

where R is the accumulated rainfall depth at time t; I_a is the initial abstraction (loss); and S is the maximum retention potential of the watershed. Considering the analysis findings from many experimental watersheds, the SCS-CN provides an empirical relationship of S and I_a, which is given as $I_a = 0.2S$. Then, the expression of R_e at a given time t becomes:

$$R_e = \frac{(R - 0.2S)^2}{R + 0.8S}, \text{ where } (R \geq 0.2S) \quad (4)$$

The maximum retention (S) can be computed as a function of the CN via the following equation.

$$S = \frac{25400 - 254CN}{CN} \quad (5)$$

In this study, 30 m spatial resolution gridded runoff CN maps were generated by considering soil and LULC characteristics (raster files), as well as the average antecedent moisture conditions (AMC-II). For the soil moisture condition, the AMC-II was accounted for because it represents a standard condition commonly used in hydrological modeling. The gridded CN maps were prepared via the ARC-GIS 10.4 environment [92]. The process involved preparing input data by aligning raster files (LULC and soil) to the same resolution, coordinate system, and extent; reclassifying LULC and HSG maps; combining them; and assigning curve numbers using a lookup table with a raster calculator. Figure 6 shows the gridded runoff curve numbers for both the historical and future periods generated based on these procedures. The results indicate that the CN values under the BAU scenario are relatively greater than those under the governance (GOV) scenario. This is attributed to the expansion of cultivated land and settlement areas under the BAU scenario. As a result, the maximum retention potential of the watershed will reduce, which may lead to an increase in peak flow occurrence due to higher surface runoff volumes. The composite CN for each subwatershed was estimated on the basis of the mean value of raster grids (pixels) within the boundaries of the subwatershed area. Similarly, the composite CN for the entire watershed was calculated as the mean value of raster grids within the boundary of the whole watershed.

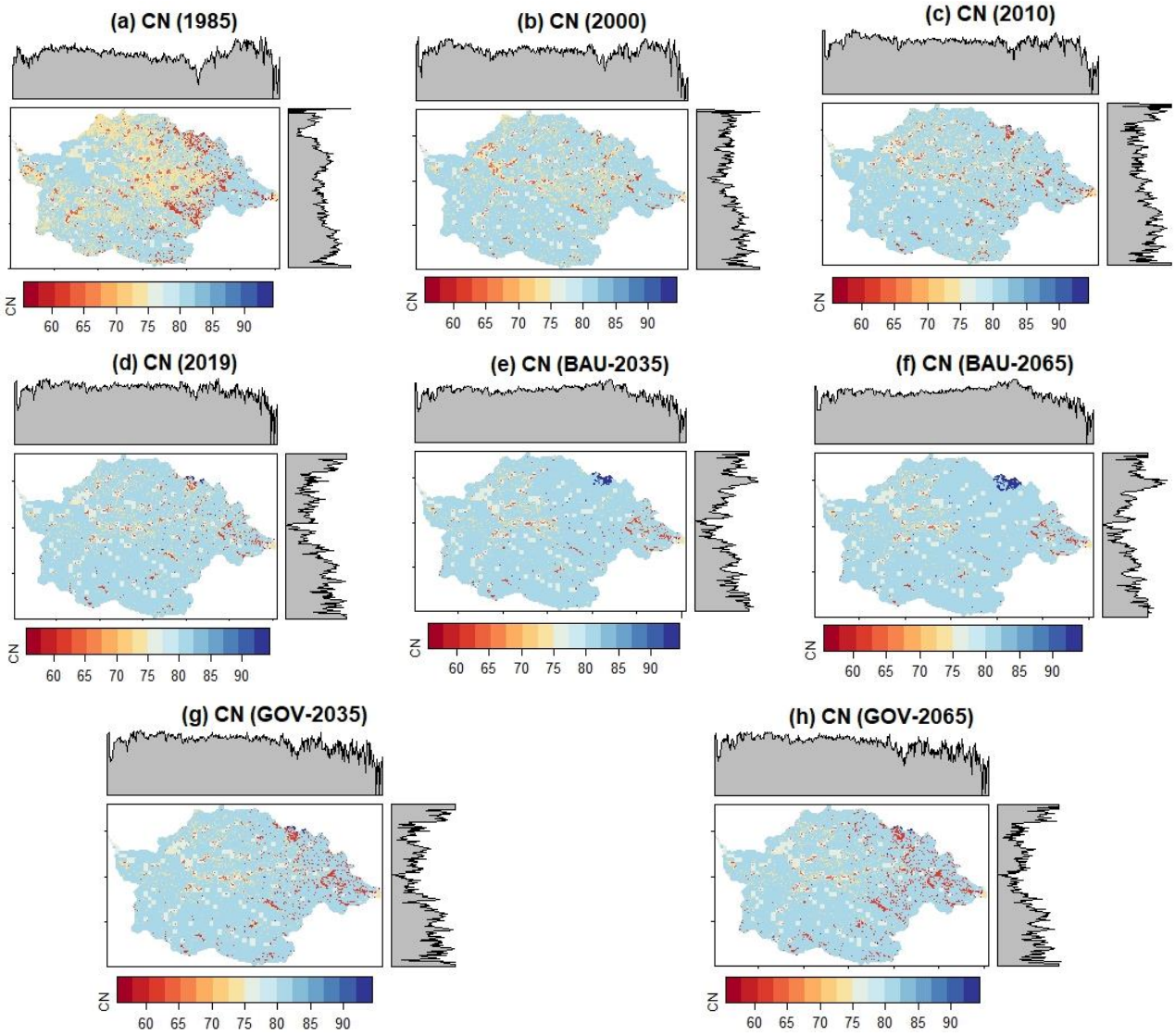

Figure 6. A 30 m spatial resolution gridded runoff curve numbers for the historical years (**a**–**d**) and future scenarios (**e**–**h**). The gray shaded areas that bound in the figure illustrate the gradient orientation of the runoff curve number, with maximum values along the north and south directions and minimum values in the middle of the watershed.

II. Direct runoff (transform model)

In the HEC-HMS model, several empirical and conceptual models are available to transform excess rainfall into direct runoff. Among these, the SCS unit hydrograph (SCS-UH) model [90] was selected for this study. The key parameter of this model is the lag time (T_{lag}), which represents the time difference between the center of mass of excess rainfall and the peak of the SCS-UH. Although the assumption of a single-peak hydrograph is a limitation of the SCS-UH, it was chosen because its parameters can be estimated from the physical characteristics of the watershed, specifically in relation to the time of concentration T_c. For this model, T_c can be computed via the Kirpich equation [93], and T_{lag} is then calculated as 0.6 times T_c:

$$T_C = 0.0195\left(L^{0.77} \Big/ S^{0.385}\right) \quad (6)$$

where T_C is the time of concentration (min.), L is the length of the longest flow path (meter), and S is the average channel slope (m/m).

III. Channel flow (routing model)

From the available flow routing models in the HEC-HMS model, the Muskingum routing model was selected for this study. This model uses a finite difference approximation of the continuity equation and is widely used for flood routing [94]. It accounts for flow attenuation resulting from the storage effect of the channel as flood flows travel through it.

The Muskingum routing model computes channel storage as follows:

$$S_t = K[XI_t + (1 - X)O_t] \tag{7}$$

where S_t, I_t, and O_t are storage, inflow, and outflow at time t, respectively; K is the travel time of the flood wave though the routing channel; and X is a dimensionless weight factor ($0 \leq X \leq 0.5$). For this study, the Muskingum routing model parameters (K and X) were determined through model calibration.

2.8.4. Model Sensitivity Analysis

Sensitivity analysis is a critical step in hydrological modeling aimed at reducing uncertainty and identifying model parameters that significantly influence the model's output [86,95]. In this study, sensitivity analysis was conducted for the parameters of the runoff volume (loss) and transform models by varying each parameter individually while keeping the others constant (local sensitivity analysis). Each parameter value was adjusted by ±25%, and the relative percentage change in peak discharge was assessed for each simulation. The sensitivity of each parameter was evaluated on the basis of the magnitude of the change in peak flow. The relative change in peak flow as a percentage was computed via the following equation:

$$Relative\ change\ (\%) = \frac{Q_{new} - Q_{base}}{Q_{base}} \times 100 \tag{8}$$

where Q_{new} is the peak flow after changing the parameter and where Q_{base} is the peak flow from the baseline simulation. In this study, model sensitivity analysis was performed for selected events that occurred from 13 to 31 August 2010.

2.8.5. Model Calibration and Validation

Model calibration and validation were performed to match the observed and simulated data for selected events. Both automated and manual calibrations were employed to obtain better agreement between the simulated and observed flow events through iterative adjustments of the model parameters. The performance of the model during calibration and validation was evaluated through graphical comparison (visual comparison) and statistical performance measures such as the coefficient of determination (R^2), Nash–Sutcliffe efficiency (NSE), root mean square error ($RMSE$), and percent bias ($PBIAS$). These performance measures were selected from different categories: R^2 from standard regression-based methods, NSE from dimensionless methods, and $RMSE$ and $PBIAS$ from error-based statistical methods [96].

R^2 expressed in Equation (9) describes the proportion of the variance in the observed data explained by the model-simulated data.

$$R^2 = \frac{\sum_{i=1}^{N} (O_i - \overline{O})(S_i - \overline{S})}{\sqrt{\sum_{i=1}^{N} (O - \overline{O})^2} \sqrt{\sum_{i=1}^{N} (S_i - \overline{S})^2}} \tag{9}$$

where O_i is the ith observed discharge value for the event being evaluated, S_i is the ith simulated discharge value for the event being evaluated, $\overline{O}$ is the mean of the observed discharge values, $\overline{S}$ is the mean of the simulated discharge values, and N is the total number

of observations. R^2 values range from 0 to 1 (inclusive), with higher values indicating less error variance, and values higher than 0.5 are generally considered acceptable values [97].

The NSE is a dimensionless statistical performance measure that describes the relative magnitude of the residual variance (noise) compared with the observed data variance (information) [98]. NSE is expressed as shown in Equation (10):

$$NSE = 1 - \frac{\sum_{i=1}^{N}(O_i - S_i)^2}{\sum_{i=1}^{N}(O_i - \overline{O})^2} \quad (10)$$

NSE ranges from $-\infty$ to 1 ($-\infty < NSE \leq 1$), where $NSE = 1$ indicates good agreement between the observed and simulated values, $0 < NSE \leq 1$ is generally considered acceptable, and $NSE \leq O$ indicates poor or unacceptable model performance.

$RMSE$ expressed in Equation (11) describes the standard deviation of the model prediction error.

$$RMSE = \sqrt{\frac{1}{N}\sum_{i=1}^{N}(O_i - S_i)^2} \quad (11)$$

The optimal value of $RMSE$ is 0, which indicates perfect agreement between the observed and simulated values.

$PBIAS$ indicates the average tendency of the model-simulated values to be higher or lower than the observed values [99]. It is given as shown in Equation (12):

$$PBIAS\ (\%) = \frac{\sum_{i=1}^{N}(O_i - S_i)}{\sum_{i=1}^{N} O_i} \times 100 \quad (12)$$

The optimal value of $PBIAS$ is 0, with low values indicating accurate model simulation. Positive $PBIAS$ values indicate overestimation, whereas negative values indicate model underestimation. According to Moriasi et al. [100], $-25\% < PBAS < 25$ is an acceptable range for discharge simulation.

In this study, model calibration was performed for two selected events: Event-1, which occurred from 1 July to 31 August 1996, and Event-2, which occurred from 5 July to 31 July 2008. Model validation was conducted via Event-3, which occurred from 2 August to 27 August 2014. These events were specifically chosen to account for periods with high flood peaks.

2.9. Flood Source Area Identification (FSAI)

Flood source area identification (FSAI) is an important approach for identifying the main sources of downstream flooding. It helps rank subwatersheds on the basis of their contribution to peak flood magnitude at the main watershed outlet. In this study, FSAI was performed using the UFR, which was introduced by Saghafian and Khosroshahi [35]. In the UFR approach, the contribution of each subwatershed can be computed as:

$$FI_n = \frac{Q_{all} - Q_{all-n}}{Q_{all}} \times 100 \quad (13)$$

$$fi_n = \frac{Q_{all} - Q_{all-n}}{A_n} \quad (14)$$

where FI_n is the gross flood index of the nth subwatershed in percent, Q_{all} is the outlet peak discharge in m^3/s when all the subawtersheds are included in the base simulation, Q_{all-n} is the outlet peak discharge in m^3/s when nth subawatersheds are excluded from the simulation, fi_n is the flood index of the nth subawtershed ($m^3/s/km^2$) based on the area of the subwatershed, and A_n is the area of the nth subwatershed in km^2.

In the UFR approach, the subwatershed with the highest flood index value is ranked first (indicating the greatest contribution to peak discharge), whereas the subwatershed with the lowest flood index value is ranked last, indicating the least contribution. In this study, a calibrated HEC-HMS model incorporating all subwatershed components was first developed. The flood indices FI and fi for each subwatershed were subsequently calculated by disconnecting or eliminating a chosen subwatershed unit while maintaining the connections of the other subwatersheds. This process was repeated for all subwatersheds, allowing for a comprehensive analysis. In this regard, the analysis was also conducted under different conditions to investigate the impacts of LULC changes on the flood index values.

2.10. Combined Impacts of LULC and Climate Change on High-Flows

The combined impacts of LULC and climate change on high flows, specifically on the annual maximum (AM) 1-day flows, were analyzed by simulating historical and future conditions using the calibrated HEC-HMS model, driven by AM 1-day rainfall. To assess these impacts on high-flow extremes, flow duration curves (FDCs) were constructed from the AM flow series. The FDC construction process involved (1) sorting AM flows in descending order, (2) ranking the AM flows, (3) calculating the probability of exceedance for each flow value, and (4) plotting the AM flow series on the y-axis against the probability of exceedance on the x-axis. In this study, the probability of exceedance was calculated using the Weibull formula:

$$P = \frac{m}{N+1} \times 100 \quad (15)$$

where P is the probability of exceedance (%), m is the rank of the flow value, and N is the total number of flow data points.

3. Results

3.1. Rainfall Climatology

3.1.1. Mean Monthly and Annual Rainfall

Figure 7 presents the mean monthly rainfall of the study watershed, estimated using both observed data and GCM-simulated rainfall data. Observed rainfall estimates were derived by merging ground-based observations with three GRFPs (MSWEP, CHIRPS, and ERA5-Land) using the RF-MERGE approach, which enhances accuracy by integrating diverse sources. Historical and future GCM-simulated rainfall estimates were derived from statistically downscaled and bias-corrected ensemble means from the CMIP5 (MIROC5, MRI-CGCM3, CanESM2, and MPI-ESM1-2-LR) and CMIP6 (MPI-ESM1-2-LR, MRI-ESM2-0, CNRM-CM6-1, and BCC-CSM2-MR) models.

Results indicate that the GCMs effectively captured observed rainfall patterns, despite projected increases in rainfall under RCP and SSP scenarios. Approximately 80% of the watershed's rainfall occurs during the main rainy season (June to September), consistent with the regional monsoon. For the historical period (1981–2005), the mean annual rainfall was estimated to be 1336 mm based on RF-MERGE data, while CMIP6 models estimated a slightly higher mean annual rainfall of 1379 mm. For future simulations, the highest projected mean annual rainfall was 1495 mm under the SSP5-8.5 scenario (2056–2080), indicating an expected increase in mean annual rainfall in the future period. These findings align with previous studies [101–103], which similarly reported projected increases in rainfall in the region.

Figure 8 illustrates the spatial distribution of mean annual rainfall (MARF) in the Gumara watershed for both the historical and future periods. The spatial distribution patterns are similar for both periods, with the primary difference being an increase in

rainfall during the future period. Overall, the mean annual rainfall in the watershed ranges from approximately 1320 mm to 1560 mm, with the highest rainfall values concentrated in the northeastern part of the watershed and the lowest rainfall occurring in the northern part (Figure 8).

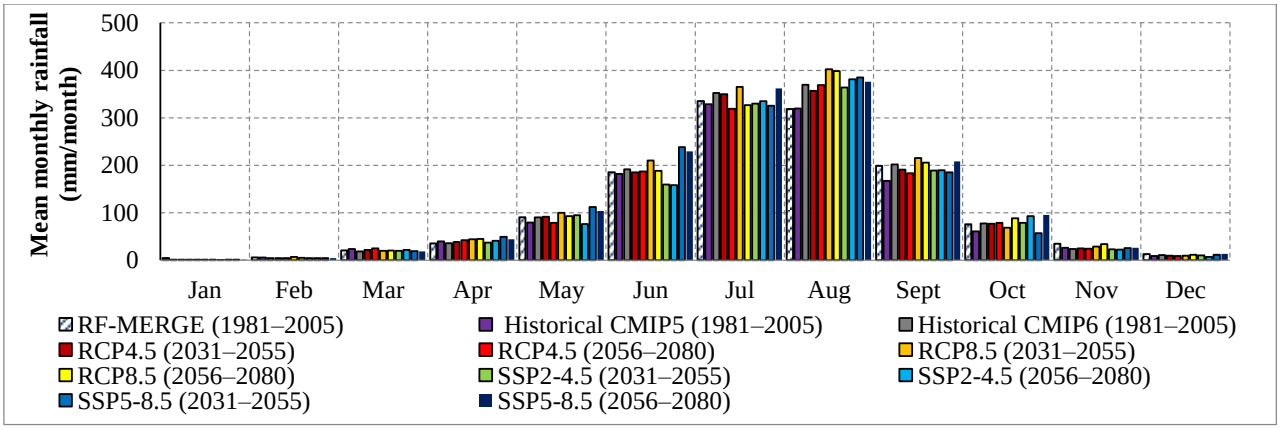

Figure 7. Historical (1981–2005) and projected (2031–2080) mean monthly rainfall (mm/month) of the Gumara watershed, estimated from RF-MERGE data and multi-model ensemble means from CMIP5 and CMIP6.

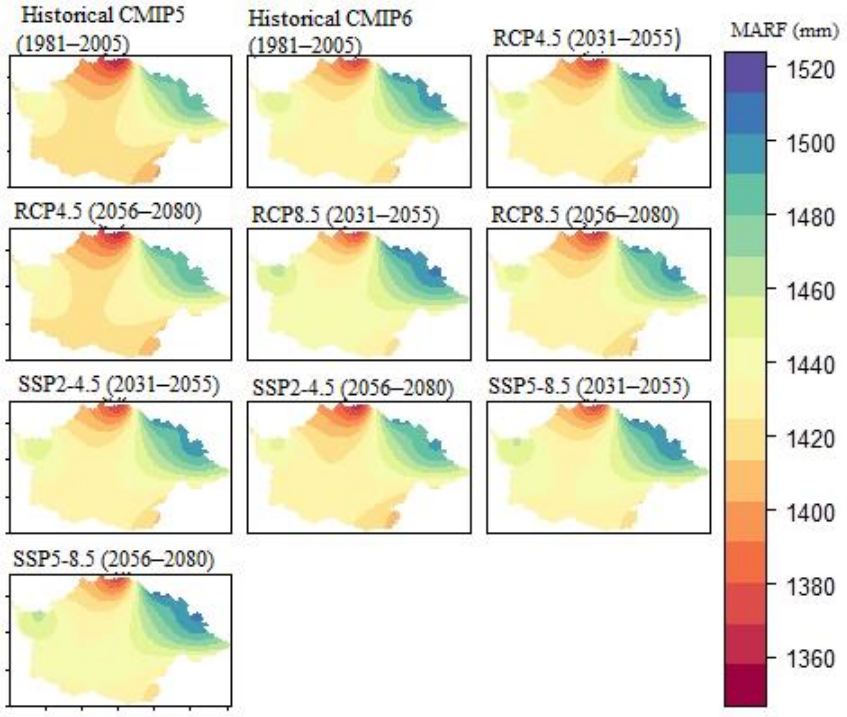

Figure 8. Spatial distribution of mean annual rainfall (MARF) in the historical (1981–2005) and two future periods, near-future (2031–2056) and far-future (2056–2080), under different climate scenarios. In the figures, different color gradients show the distribution of rainfall in the study area, where the dark blue color grade shows areas that receive the highest mean annual rainfall.

3.1.2. Design Rainfall and Depth–Duration–Frequency (DDF) Curve

Design rainfall for the study watershed for various return periods was estimated by fitting the AM 1-day rainfall extracted from RF-MERGE estimates (Figure 9a) to candidate distributions. The goodness-of-fit test identified the GEV distribution as the best fit. Consistent with this finding, similar studies [104,105] have reported the reliability of the GEV distribution for predicting extreme rainfall indices, such as the AM 1-day rainfall.

The estimated design rainfall values for a 1-day duration using the GEV distribution were 70 mm, 75 mm, 81 mm, 85 mm, and 88 mm for the 5-, 10-, 25-, 50-, and 100-year return periods, respectively. However, to analyze flood occurrence, shorter-duration rainfall depths are often required for hydrological models. For this, a DDF curve for a 1-h duration was developed using a regional equation. Figure 9b presents this DDF curve, which predicts extreme rainfall intensity over various durations and return periods.

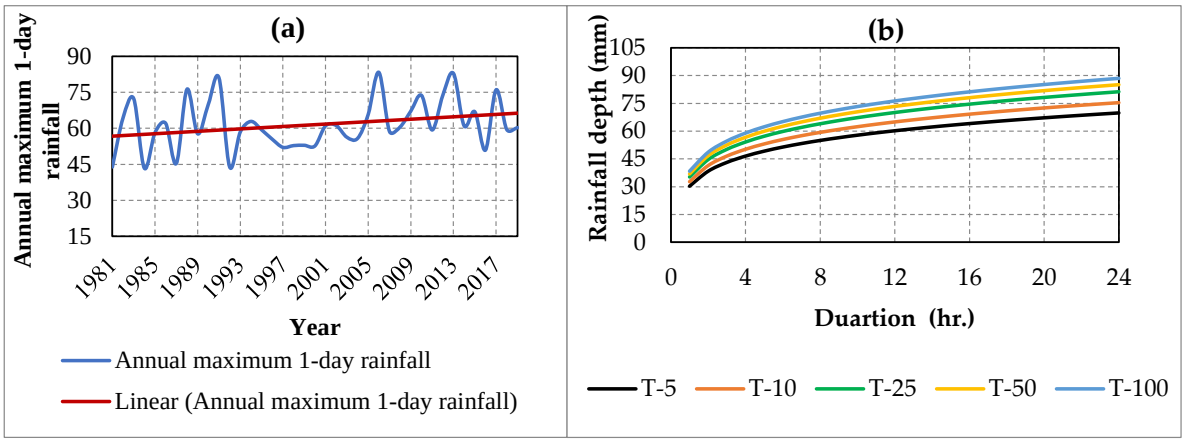

Figure 9. (**a**) Temporal variation of the long-term annual maximum (AM) 1-day rainfall series from RF-MERGE estimates (1981–2019) and (**b**) depth–duration–frequency (DDF) curve developed from RF-MERGE rainfall. In panel (**a**), the red line illustrates the increasing linear trend of annual maximum 1-day rainfall.

3.1.3. Annual Maximum (AM) 1-Day Rainfall

The historical and projected annual maximum 1-day rainfall series were extracted from CMIP5 and CMIP6 multimodal ensemble means. The extracted 1-day rainfall was converted to hourly distributed rainfall using a regional equation and subsequently used to simulate the annual maximum flow series. The box plot in Figure 10 illustrates the distribution of the extracted data. As shown, the data exhibit high variability across all periods, with an increase in future periods relative to historical values. Across all periods, the extracted maximum 1-day rainfall ranges from 23 mm to 83 mm, with the highest values observed under the SSP climate scenarios.

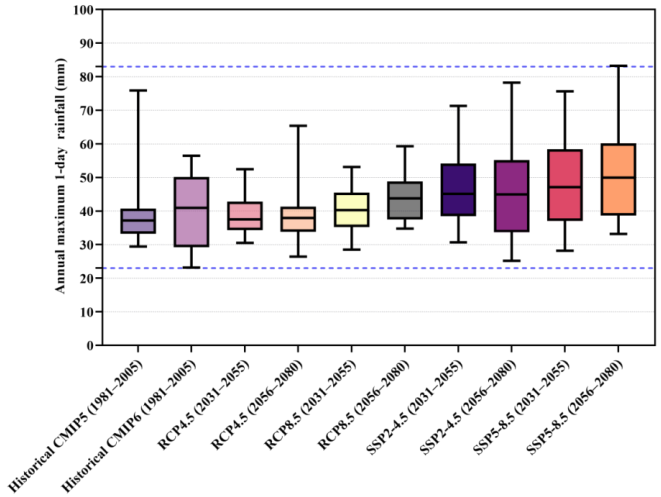

Figure 10. Box plot of historical (1981–2005) and projected (2031–2080) annual maximum (AM) 1-day rainfall, represented in different color. The plot summarizes the minimum, first quartile (Q1), median, third quartile (Q3), and maximum values of the rainfall data. The blue dashed lines indicate the full range of data (minimum and maximum values) across the study periods.

3.2. Land Use and Land Cover Change Analysis

LULC maps of the study watershed for the historical (1985, 2000, 2010, and 2019) and future (2035 and 2065) years were extracted from our previous work [26], which analyzed the entire Gumara watershed. Figure 11a,b present the percentage coverage of different LULC classes for both the historical and future years, respectively. During the historical period, a significant increase in cultivated land and settlements was observed at the expense of a decrease in other land use classes. From 1985 to 2019, the percentage area of cultivated land and settlements increased from 63.70% (800.07 km^2) to 88.39% (1110.18 km^2) (Figure 11a). In contrast, the percentage areas of forest, shrubland, and grassland decreased from 4.98%, 28.21%, and 2.35% to 1.97%, 7.88%, and 0.59%, respectively (Figure 11a). These findings align with previous studies by Anteneh and Mohammed [106] and Chakilu and Moges [107], which also reported an increase in agricultural cultivation in the region.

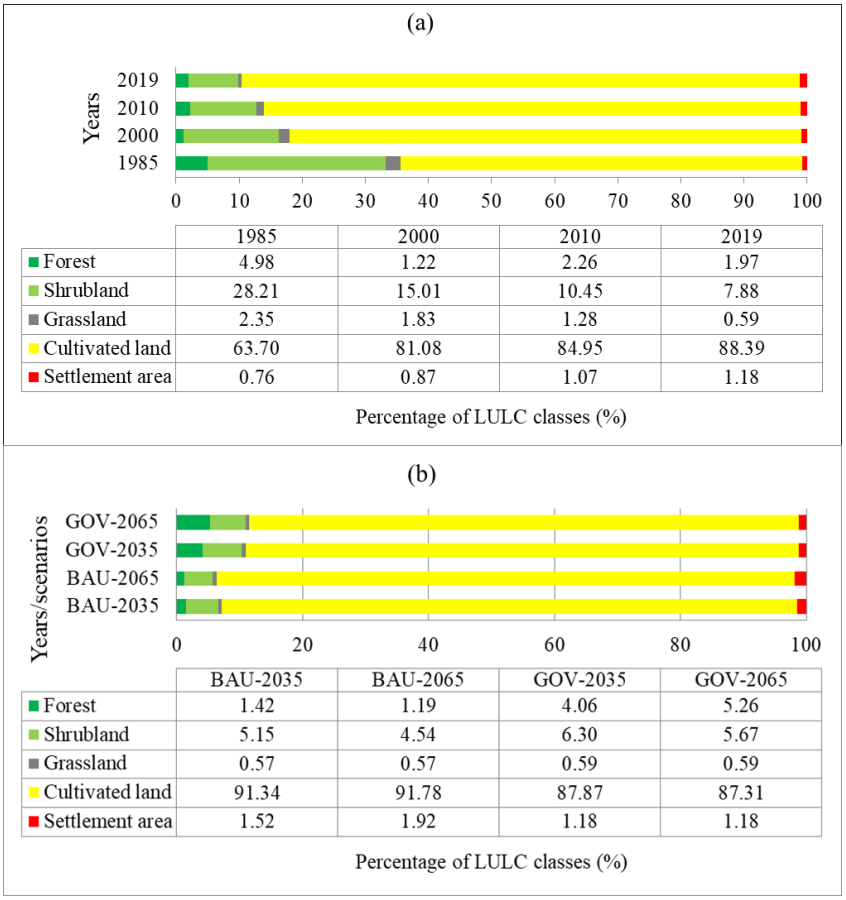

	1985	2000	2010	2019
Forest	4.98	1.22	2.26	1.97
Shrubland	28.21	15.01	10.45	7.88
Grassland	2.35	1.83	1.28	0.59
Cultivated land	63.70	81.08	84.95	88.39
Settlement area	0.76	0.87	1.07	1.18

	BAU-2035	BAU-2065	GOV-2035	GOV-2065
Forest	1.42	1.19	4.06	5.26
Shrubland	5.15	4.54	6.30	5.67
Grassland	0.57	0.57	0.59	0.59
Cultivated land	91.34	91.78	87.87	87.31
Settlement area	1.52	1.92	1.18	1.18

Figure 11. Percentage coverage of land use and land cover (LULC) classes of the Gumara watershed. (**a**) Historical years (1985, 2000, 2010, and 2019) and (**b**) future years (2035 and 2065) under the business-as-usual (BAU) and governance (GOV) scenarios.

Figure 11b shows the predicted percentage area of each LULC class in the study watershed for the years 2035 and 2065 under the BAU and GOV scenarios. Under the BAU scenario (which is based on the current trend of LULC change), cultivated land is expected to dominate, covering 91.34% and 91.78% of the area in 2035 and 2065, respectively, at the expense of decreases in other LULC classes (forest, shrubland, and grassland). Conversely, under the GOV scenario (which is based on the green legacy initiative program), forest cover is predicted to increase, reaching 50.98 km^2 (4.06%) in 2035 and 66.06 km^2 (5.26%) in 2065. In this scenario, the expansion of cultivated land will be more controlled than in the BAU scenario. These findings are consistent with a study conducted in the upper Awash

basin of Ethiopia by Gebresellase et al. [27], which indicated an increase in agricultural lands and settlements under the BAU scenario and improvements in forests under the GOV scenario.

3.3. Hydrological Modeling

3.3.1. Delineated Subwatersheds

Accounting for the homogeneity of various watershed characteristics, such as soil, LULC, elevation, and stream networks the Gumara watershed was delineated into eight subwatersheds, labeled W1 to W8 (Figure 12). The area of the subwatersheds ranges from 99.9 km^2 (W6) to 215 km^2 (W4) (Figure 12). Table 4 also presents the computed subwatershed (area and slope) and stream characteristics (length and slope).

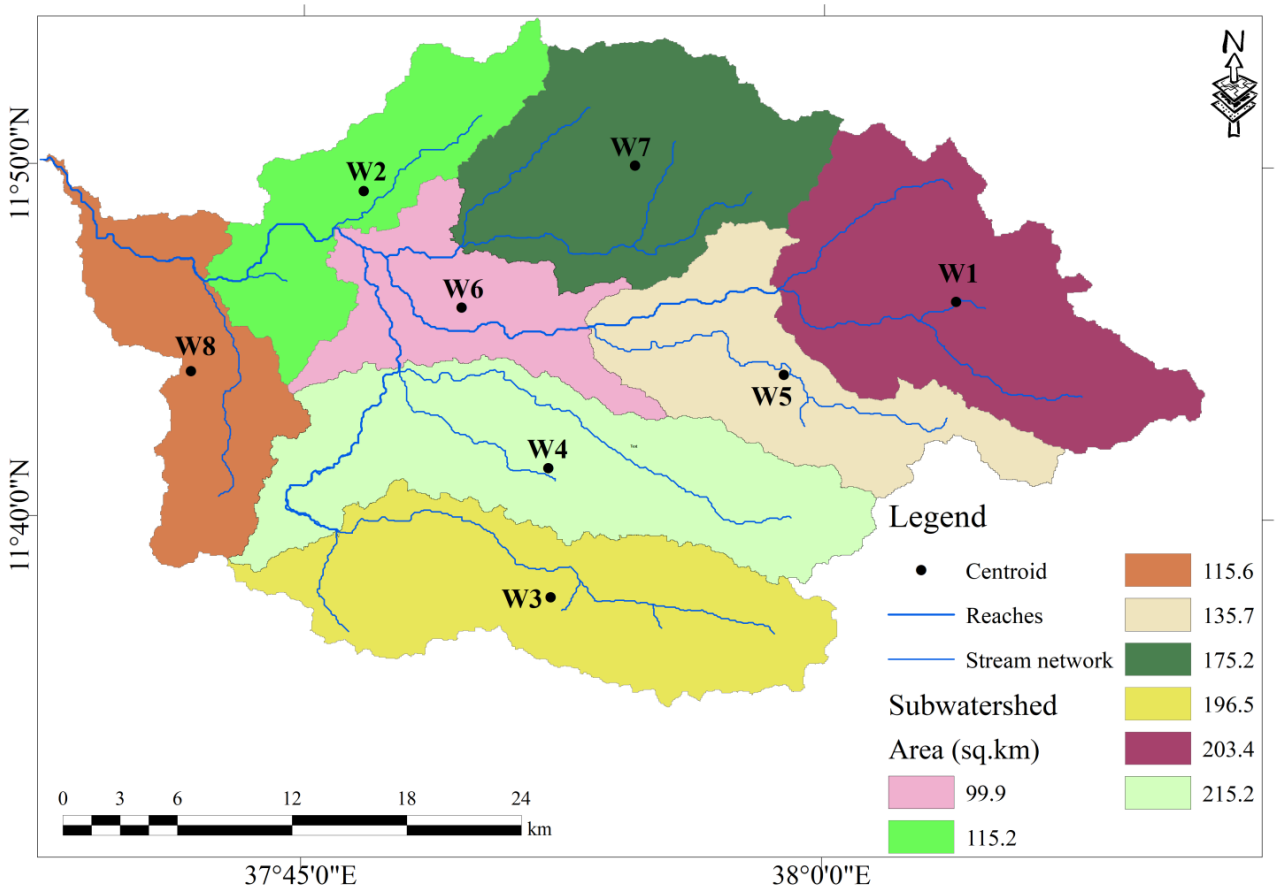

Figure 12. Delineated subwatershed's area, centroids, and stream network of the Gumara watershed as delineated in the HEC-HMS model.

Table 4. Characteristics of subwatersheds (area, slope, longest flow path length and slope, centroidal flow path length and slope, and drainage density).

Subwatershed	Area (km^2)	Subwatershed Slope (%)	Longest Flow Path Length (km)	Longest Flow Path Slope (%)	Centroidal Flow Path Length (km)	Centroidal Flow Path Slope (%)
W1	203.4	24.20	30.8	4.952	11.4	1.89
W2	115.2	13.10	28.9	1.748	13.3	0.35
W3	196.5	15.00	34.0	1.39	14.2	1.13
W4	215.2	19.40	34.2	2.287	13.0	1.06
W5	135.7	24.20	35.9	3.118	15.1	1.94
W6	99.9	14.50	25.8	1.871	10.3	0.18
W7	175.2	19.70	27.2	2.936	10.0	1.10
W8	115.6	15.40	33.6	1.999	21.0	0.97
Gumara	1256.7					

3.3.2. Model Sensitivity Analysis

Sensitivity analysis was performed to prioritize parameters for calibration and improve model efficiency. In this study, sensitivity analysis of the HEC-HMS model was conducted on key parameters, including CN, which controls runoff volume; I_a, which influences the proportion of rainfall lost before runoff begins; and T_{lag}, which affects the timing of peak discharge. For this analysis, flow events from 13 August to 31 August 2010 were considered (Figure 13). The results indicate that the CN was the most sensitive parameter. A direct relationship between flow and the CN was observed: increasing the CN resulted in higher discharge, while decreasing the CN led to lower discharge. Specifically, a 25% increase in the CN led to a 9.79% rise in peak discharge, while a 25% decrease in the CN caused a 12.71% reduction in peak discharge (Table 5). These findings are consistent with studies by Tassew et al. [89] in the Gilgel Abay catchment and Zelelew and Melesse [108] in a small watershed in northwest Ethiopia, both of which also identified the CN as the most sensitive parameter. In contrast, I_a and T_{lag} were less sensitive, with minimal impact on peak discharge. Furthermore, since the SCS-CN method assumes uniform soil, land use, and rainfall conditions within a subwatershed, the model output (runoff volume) may be subject to uncertainties in watersheds with diverse topography, such as varying slopes and elevations. To address this limitation, it is crucial to adjust CN to local conditions based on field surveys and topographic data.

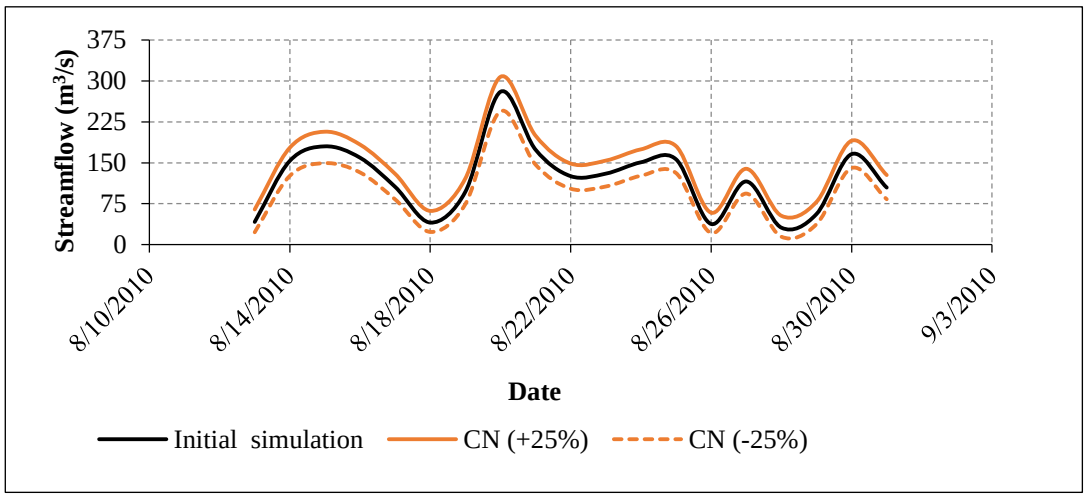

Figure 13. Model sensitivity analysis for the runoff curve number (CN) from 13 August to 31 August 2010.

Table 5. Changes in peak discharge due to changes in the runoff curve number (CN) with ±25% for selected events (from 13 August to 31 August 2010).

Simulation	Peak Discharge (m^3/s)	Change in Peak Discharge (%)
Initial simulation	280	–
CN (+25%)	307.4	9.79
CN (−25%)	244.4	−12.71

3.3.3. Model Calibration and Validation

Model calibration and validation were performed for selected events. These events were chosen on the basis of the availability of gap-free discharge data and discharge series with high flood peaks. Figure 14 presents a comparison of the observed and simulated discharge hydrographs for these selected events.

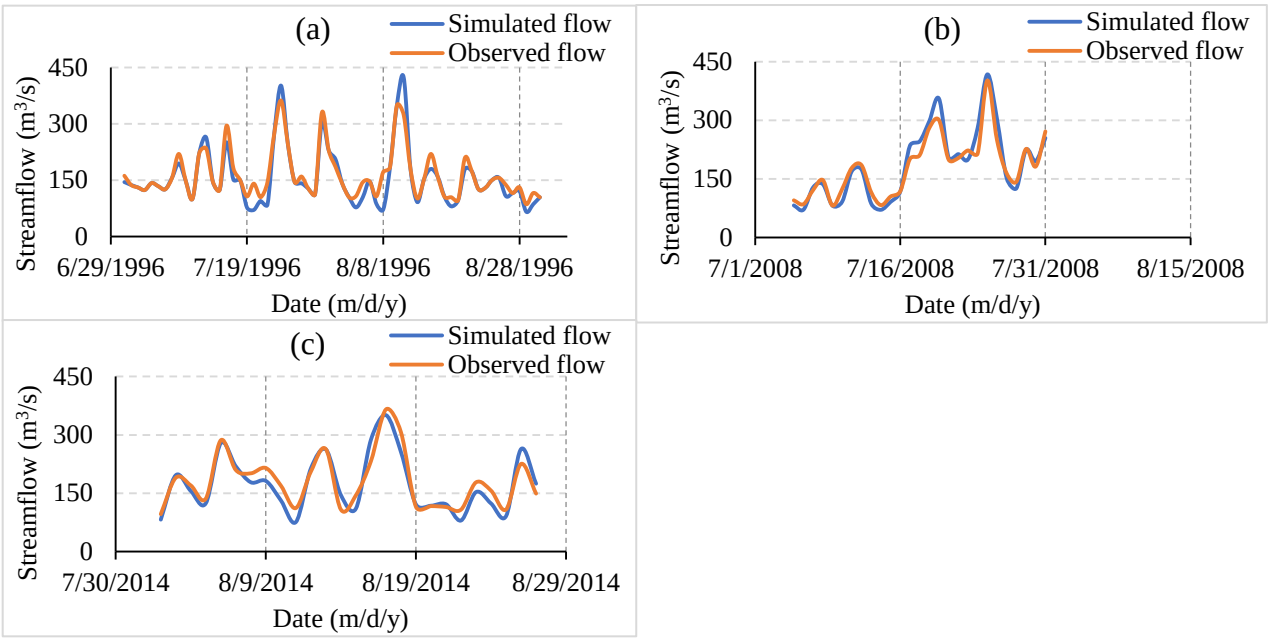

Figure 14. Observed and simulated discharge for selected events: (**a**) Event 1 (calibration), from 1 July to 31 August 1996; (**b**) Event 2 (calibration), from 5 July to 31 July 2008; (**c**) Event 3 (validation), from 2 August to 27 August 2014.

In flood modeling, the most critical aspect of the hydrograph is the peak discharge, as it is the peak that has the potential to cause flooding downstream. In this study, the model adequately captured the timing of the hydrograph peaks, although it tended to slightly overestimate peak discharge during calibration and underestimate during validation (Figure 14 and Table 6).

Table 6. Model performance evaluation during calibration and validation.

Event	Peak Discharge (m^3/s)		Performance Evaluation			
	Observed	Simulated	RMSE (m^3/s)	R	NSE	PBIAS
Event 1 (calibration)	362	423.6	27.1	0.89	0.82	−5.19
Event 2 (calibration)	402	417.7	25.69	0.94	0.88	1.95
Event 3 (validation)	365.5	350.8	26.70	0.87	0.85	−3.99

Table 6 summarizes the observed and simulated peak discharge and model performance evaluation results during the calibration and validation periods in terms of R^2, NSE, $RMSE$, and $PBIAS$. The observed and simulated discharges were in close agreement. For example, an R^2 value of 0.89, NSE value of 0.82, $RMSE$ value of 27.1 m^3/s, and $PBIAS$ value of −5.19% were found for Event 1 (calibration). Like during the calibration period, the observed and simulated discharges closely agreed during the validation period (Event 3), with R^2 value of 0.87, NSE value of 0.85, $RMSE$ value of 26.7 m^3/s, and $PBIAS$ value of −3.99%. According to Moriasi et al. [100], the statistical performance measures computed in this study are within an acceptable range, as the R^2 and NSE values exceed 0.5, and the $PBIAS$ values fall within ±25% for all events, indicating minimal error. Similarly, previous studies have demonstrated the effectiveness of the HEC-HMS model in simulating discharge in the UBN basin of Ethiopia. For instance, Tassew et al. [89] applied HEC-HMS in the Gilgel Abay catchment, UBN basin of Ethiopia, and achieved R^2 values between 0.68 and 0.95 and NSE values ranging from 0.63 to 0.92 during calibration and validation for selected flow events, indicating acceptable model performance. Similarly, Yilma and Kebede [109] used HEC-HMS in the Dabus subbasin, achieving calibration results with

R^2 = 0.81 and *NSE* = 0.78, while validation yielded R^2 = 0.87 and *NSE* = 0.79, indicating the reliability of the HEC-HMS model for rainfall–runoff simulations. These findings suggest that the HEC-HMS model can reliably simulate discharge in watersheds with topographic, soil, and LULC characteristics similar to the Gumara watershed. Table 7 also presents the calibrated (optimal) parameter values of the HEC-HMS model for the runoff volume (loss), direct runoff (transform), and routing components. These calibrated parameter values fall within the acceptable ranges specified in the HEC-HMS Technical Reference Manual [110].

Table 7. Calibrated model parameter values for the runoff volume, direct runoff, and routing models.

Runoff Volume Model: SCS-Curve Number			Direct Runoff Model: SCS-Unit Hydrograph		Routing Model: Muskingum Model		
Subwatershed	**Initial Abstraction (mm)**	**Curve Number**	**Subwatershed**	**Lag Time (min.)**	**Reach**	**Muskingum K (hr.)**	**Muskingum X (hr.)**
W1	15.2	77	W1	106	R1	1	0.45
W2	14.9	77	W2	150	R2	0.76	0.50
W3	14.3	78	W3	186	R3	0.15	0.35
W4	14.3	78	W4	155	R4	0.1	0.30
W5	14.9	77	W5	142	R5	0.58	0.50
W6	15.5	77	W6	134	R6	1.1	0.50
W7	15.2	77	W7	118	R7	1.17	0.45
W8	14.3	78	W8	160	R8	0.36	0.40

3.4. Return Period-Based Peak Discharge and Runoff Volume Simulation

Flood and runoff volume hydrographs were simulated in the calibrated HEC-HMS model. Figure 15a,b compare the peak discharge and total runoff volume of simulated hydrographs under different LULC conditions based on DDF curves of different return periods. From the results, increases in peak discharge and runoff volume were observed in the study watershed from 1985 to 2019. Among the simulation results, maximum peak discharge values of 211.7, 278.5, 359.5, 416.7, and 452.7 m^3/s were found for the 5-, 10-, 25-, 50-, and 100-year return periods, respectively, under LULC-2019 (Figure 15a). For the same period, runoff volume values of 5.9, 7.6, 9.6, 11.05, and 11.7 mega cubic meters (MCM) were found for the respective return periods (Figure 15b).

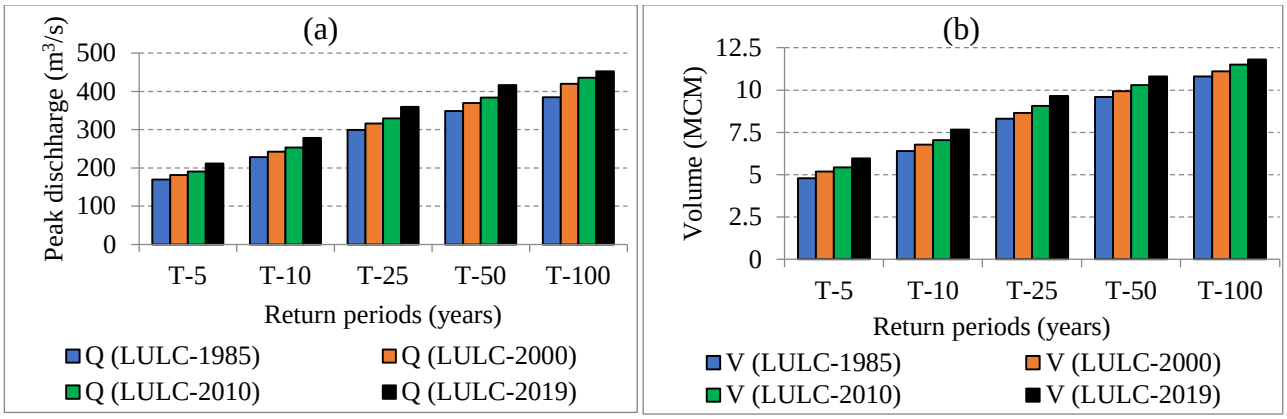

Figure 15. (**a**) Comparison of simulated peak discharge (Q) under various land use conditions across different return periods and (**b**) comparison of simulated runoff volume (V) under various land use conditions across different return periods.

Historical observations from 1981 to 2019 indicate that the average peak flood magnitude of the Gumara River was approximately 260.0 m^3/s, closely matching the simulated peak flood magnitudes for the 5- and 10-year return periods. The simulated results also

align with historical flood events recorded during the main rainy months (July and August) in 1996, 2006, 2008, 2014, and 2019, which caused significant inundation of cultivated lands and rural settlements downstream of the Gumara watershed [45,111]. Furthermore, previous studies [30,47] that employed at-site flood-frequency analysis within the Gumara watershed reported peak flood magnitudes comparable to the simulated results of this study.

Table 8 also shows the relative changes in peak discharge and runoff volume between two different LULC conditions (LULC-1985 to LULC-2019). The results indicate that the relative effect of LULC change decreases in flood peaks and runoff volumes of higher return periods, which is consistent with previous studies [34,112,113]. For example, the LULC change from 1985 to 2019 increased the peak discharge by 38.7% for a 5-year return period but only by 22.4% for a 100-year return period. Similarly, the LULC change from 1985 to 2019 increased the runoff volume by 24.9% for a 5-year return period but only by 17.6% for a 100-year return period. This could be due to the diminishing impact of land use changes for higher return periods, such that further increases in rainfall do not significantly affect peak discharge [39]. The analysis results also show that the impact of LULC change is more noticeable on peak discharge than on runoff volume.

Table 8. Changes in peak discharge and runoff volume for different return periods between LULC-1985 and LULC-2019.

Return Period	Peak Discharge (m^3/s)			Runoff Volume (MCM)		
	1985	2019	Change (%)	1985	2019	Change (%)
T-5	169.4	211.7	24.9	4.8	5.96	24.2
T-10	228.4	278.5	21.9	6.4	7.66	19.7
T-25	298.9	359.5	20.2	8.3	9.66	16.4
T-50	348.4	416.7	19.6	9.6	10.8	12.5
T-100	384.8	452.7	17.6	10.8	11.8	9.3

Historical observations from 1981 to 2019 indicate that the average peak flood magnitude of the Gumara River was approximately 260 m^3/s, which aligns closely with the simulated peaks for the 5- and 10-year return periods of LULC-2019. The simulated return period-based peak flood magnitudes are also consistent with historical flood events recorded during the main rainy months (July and August) in the years 1996, 2006, 2008, 2014, and 2019. These events resulted in substantial inundation of cultivated lands and rural settlements downstream of the Gumara watershed.

3.5. Flood Source Area Identification

The ranking of subwatersheds on the basis of their contribution to peak discharge at the main outlet of the Gumara watershed was determined via the UFR approach [35]. In this analysis, peak discharge was simulated in the calibrated HEC-HMS model using the DDF curve of the 50-year return period. Table 9 presents the peak discharge contributions and rankings of subwatersheds under different LULC conditions. According to column 3 in Table 9, subwatershed W1 generated the highest peak discharge values under LULC-1985 and 2000 (74.9 and 81.8 m^3/s, respectively). In contrast, subwatersheds W2 and W6 generated the smallest peak discharge values under the respective LULC conditions (37.5 and 39.9 m^3/s, respectively). Under LULC-2010 and 2019, subwatershed W4 generated the largest peak discharge values (84.6 and 90.7 m^3/s, respectively), whereas W6 (42.9 m^3/s) and W2 (51.4 m^3/s) generated the smallest peak discharge values for the respective LULC conditions.

Table 9. Comparison of 50-year peak discharge generation in the Gumara watershed under different land use conditions.

Subwatershed	Area (km^2)	Q_n (m^3/s)	Q_{all-n} (m^3/s)	FI_n(%)	Priority Based on FI_n	fi_n (m^3/s/km^2)	Priority Based on fi
LULC-1985							
W1	203.4	74.9	270.7	16.8	2	0.269	3
W2	115.2	37.5	297.5	8.6	7	0.242	6
W3	196.5	65.6	281.5	13.5	4	0.223	8
W4	215.2	67	266.5	18.1	1	0.274	2
W5	135.7	40.1	292.4	10.1	5	0.243	5
W6	99.9	42	295.1	9.3	6	0.303	1
W7	175.2	55.7	281.4	13.5	3	0.251	4
W8	115.6	40.6	298.9	8.1	8	0.229	7
Gumara	1256.7	325.4					
LULC-2000							
W1	203.4	81.8	310.8	15.8	2	0.287	5
W2	115.2	40.5	338.1	8.4	7	0.269	7
W3	196.5	69.6	324.1	12.2	4	0.229	8
W4	215.2	80.6	298.5	19.1	1	0.328	1
W5	135.7	50.8	328.8	10.9	5	0.297	4
W6	99.9	39.9	338.6	8.3	8	0.305	3
W7	175.2	73.4	313.2	15.1	3	0.319	2
W8	115.6	50.2	337	8.7	6	0.278	6
Gumara	1256.7	369.1					
LULC-2010							
W1	203.4	82.6	324.8	15.3	2	0.289	7
W2	115.2	45.5	348.7	9.1	6	0.303	5
W3	196.5	70.3	339.1	11.6	4	0.226	8
W4	215.2	84.6	309.6	19.3	1	0.344	1
W5	135.7	54.8	340.3	11.3	5	0.319	4
W6	99.9	42.9	350.4	8.7	8	0.332	3
W7	175.2	75.4	325.5	15.1	3	0.333	2
W8	115.6	51.1	350	8.8	7	0.291	6
Gumara	1256.7	383.6					
LULC-2019							
W1	203.4	89.7	352.8	15.3	3	0.314	6
W2	115.2	51.4	378.1	9.3	6	0.335	5
W3	196.5	76.6	369.1	11.4	5	0.242	8
W4	215.2	90.7	337.5	19.0	1	0.368	1
W5	135.7	61.1	368.6	11.5	4	0.354	4
W6	99.9	48.3	380.1	8.8	7	0.366	3
W7	175.2	83.4	352.3	15.5	2	0.367	2
W8	115.6	53	381.7	8.4	8	0.303	7
Gumara	1256.7	416.7					

where Q_n is the peak discharge (m^3/s) for the *nth* subawatershed, Q_{all-n} is the peak discharge (m^3/s) when the *nth* subawatershed is excluded from the simulation, FI_n is the gross flood index of the *nth* subwatershed (%), and fi_n is the flood index of the *nth* subawtershed (m^3/s/km^2).

Additionally, subwatershed units or (flood source areas) were ranked on the basis of flood index values such as FI and fi (Table 9). According to the results, different ranking index values were found under different conditions. For example, under LULC-1985, the W2 subwatershed, which is seventh in terms of area and eighth in terms of peak discharge generation, acquired seventh and sixth ranks in terms of the FI and fi indices, respectively (Table 9, columns 2, 3, 6, 8). While it maintains the same FI rank under LULC-2000, it jumps to seventh in terms of the fi index. Similarly, under LULC-2010, the W8 subwatershed, which is sixth in terms of area and peak discharge generation, acquired the seventh rank in the FI index and sixth rank in the fi index (Table 9, columns 2, 3, 6, 8). However, it jumps to eighth and seventh ranks in terms of the FI and fi indices, respectively, under LULC-2019.

Furthermore, previous studies [39,113] recommend the fi index for ranking because it considers changes in peak discharge per unit area, unlike the FI index, which considers only changes in peak discharge. Therefore, more attention needs to be given to subwatersheds with high fi index values during prioritization to reduce runoff generation in these subwatersheds. Figure 16 shows the fi index of each subwatershed of the Gumara watershed for the baseline period. According to the results, W6 was the most runoff-generating subwatershed under LULC-1985, with a fi index value of 0.303, whereas W4 was the most runoff-generating subwatershed under LULC conditions of 2000, 2010, and 2019, with fi index values of 0.328, 0.34, and 0.368, respectively. These show the combined effects of LULC and other related factors such as the location of subwatersheds within the entire watershed, river routing, elevation, slope, LULC, stream network, reach length and slope, rainfall distribution, and other physical features of the watershed under study in prioritizing subwatersheds [36,113,114]. The combined effects of these factors can be well simulated via hydrologic models such as the HEC-HMS model used in this study.

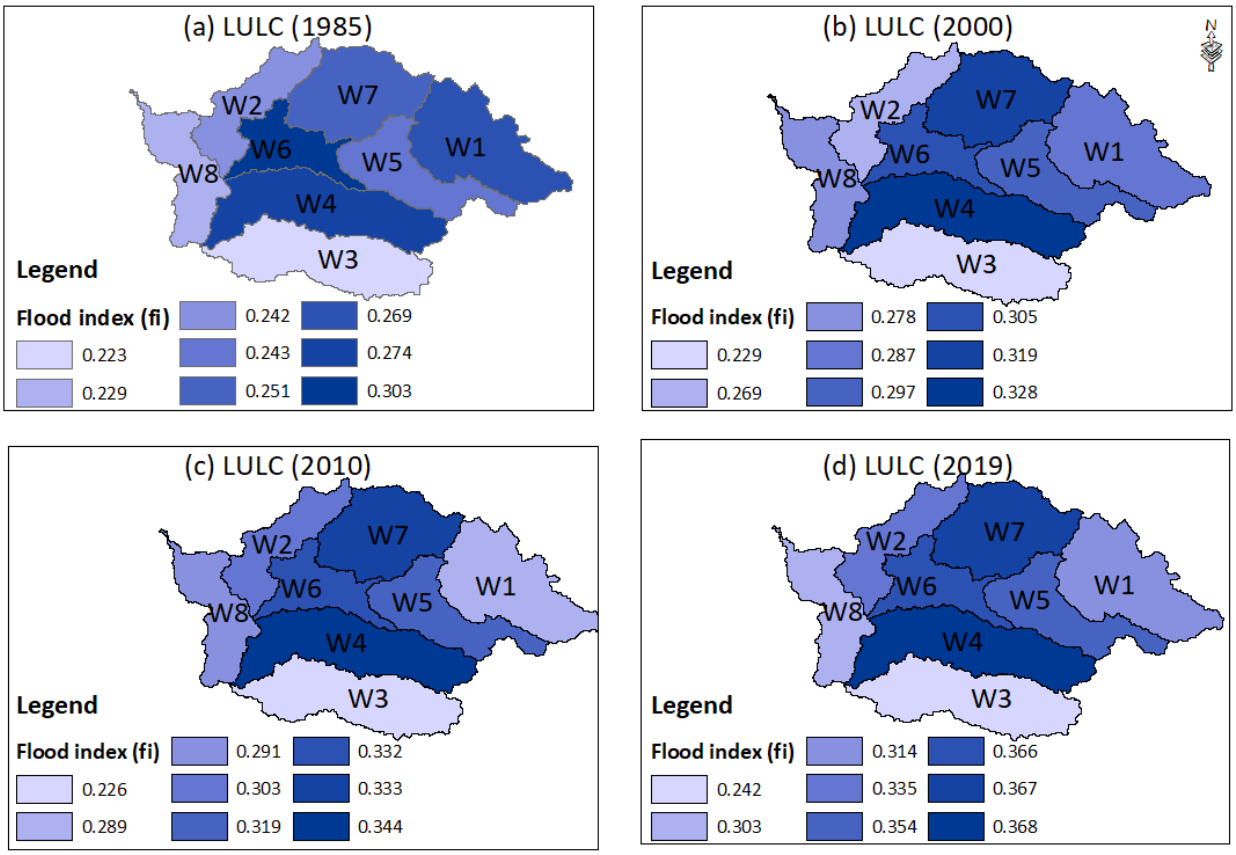

Figure 16. Computed flood index (fi) values estimated using the Unit Flood Response (UFR) approach for a 50-year return period peak discharge under different LULC conditions: (**a**) LULC-1985, (**b**) LULC-2000, (**c**) LULC-2010, and (**d**) LULC-2019. The blue color gradient represents flood index levels across subwatersheds, with the darkest blue indicating subwatersheds with the highest runoff potential.

3.6. Combined Impacts of LULC and Climate Change on High Flows

Historical and projected high flows of the study watershed were simulated using the calibrated HEC-HMS model, based on the AM 1-day rainfall. Table 10 below presents the mean AM flows, along with relative percentage change values. The results indicate that greater high-flow magnitudes were observed when future climate scenarios were combined with the BAU land use scenario compared to the GOV scenario. Specifically, the highest flow value of 254.8 m^3/s was found under the combined BAU-2065 land use and SSP5-8.5

(2056–2080) climate scenario, while the highest value of 230.6 m^3/s was found under the combined GOV-2065 land use and SSP5-8.5 (2056–2080) climate scenario (Table 10).

Table 10. Change in high flow of the Gumara watersheds under combined climate (RCP and SSP) and land use (BAU-2035, BAU-2065, GOV-2035, and GOV 2065) scenarios.

Scenario/Period	BAU Land Use Scenario	Flow Under Combined Future Climate and BAU Land Use Scenario		GOV Land Use Scenario	Flow Under Combined Future Climate and GOV Land Use Scenario	
		Mean Annual Maximum Flow (m^3/s)	Change (%)		Mean Annual Maximum Flow (m^3/s)	Change (%)
Historical CMIP5 (1981–2005)		188.1	–		188.1	–
Historical CMIP6 (1981–2005)		211.5	–		211.5	–
RCP4.5 (2031–2055)	2035	224	19.1	2035	200.5	6.6
RCP4.5 (2056–2080)	2065	209.4	11.3	2065	200.2	6.4
RCP8.5 (2031–2055)	2035	223.5	18.9	2035	204.0	8.5
RCP8.5 (2056–2080)	2065	225.7	20.0	2065	202.8	7.8
SSP2-4.5 (2031–2055)	2035	243.1	14.9	2035	225.1	6.4
SSP2-4.5 (2056–2080)	2065	237.4	12.3	2065	223.9	5.9
SSP5-8.5 (2031–2055)	2035	246.4	16.5	2035	226.4	7.0
SSP5-8.5 (2056–2080)	2065	254.8	20.5	2065	230.6	9.0

Considering the relative change values, higher positive change values were observed when future climate scenarios combined with the BAU scenario ranged from 11.3% to 20.5% (Table 10). Among the computed changes under the BAU scenario, the greatest increase is projected under SSP5-8.5 (2056–2080) with a 20.5% increment. These significant increases in high flows in the future suggest a higher likelihood of more frequent flooding in the region.

In contrast, the change values are smaller when future climate scenarios are combined with the GOV land use scenario (Table 10), ranging from 5.9% to 9.0%. Among the computed changes under the GOV scenario, the greatest increase is projected under SSP5-8.5 (2056–2080) with a 9.0% increment. These lower change values can likely be attributed to afforestation efforts and controlled cultivation under the GOV scenario, which could enhance infiltration, reduce surface runoff, and contribute to more stable streamflow, especially during extreme rainfall events.

Furthermore, flow duration curves (FDCs) were constructed to assess the combined impact of LULC and climate change on high flows (Figure 17a,b). The results showed significant variations of high flows, particularly when different climate scenarios combined with the BAU land use scenario (Figure 17a) than combined with the GOV scenario (Figure 17b). The change in the high flow of the study watershed was also assessed by classifying high flow magnitudes into four categories depending on different ranges of probability of exceedance (Q0–Q25, Q26–Q50, Q51–Q75, and Q76–Q100) (Table 11). Based on these categories, the change in high flow is more visible in the Q0–Q25. In this category (Q0–Q25), the SSP5-8.5 (2056–2080) scenario showed greater change in high flow when combined with the BAU-2065 and GOV-2065 land use scenarios as shown in Figure 17a and 17b, respectively.

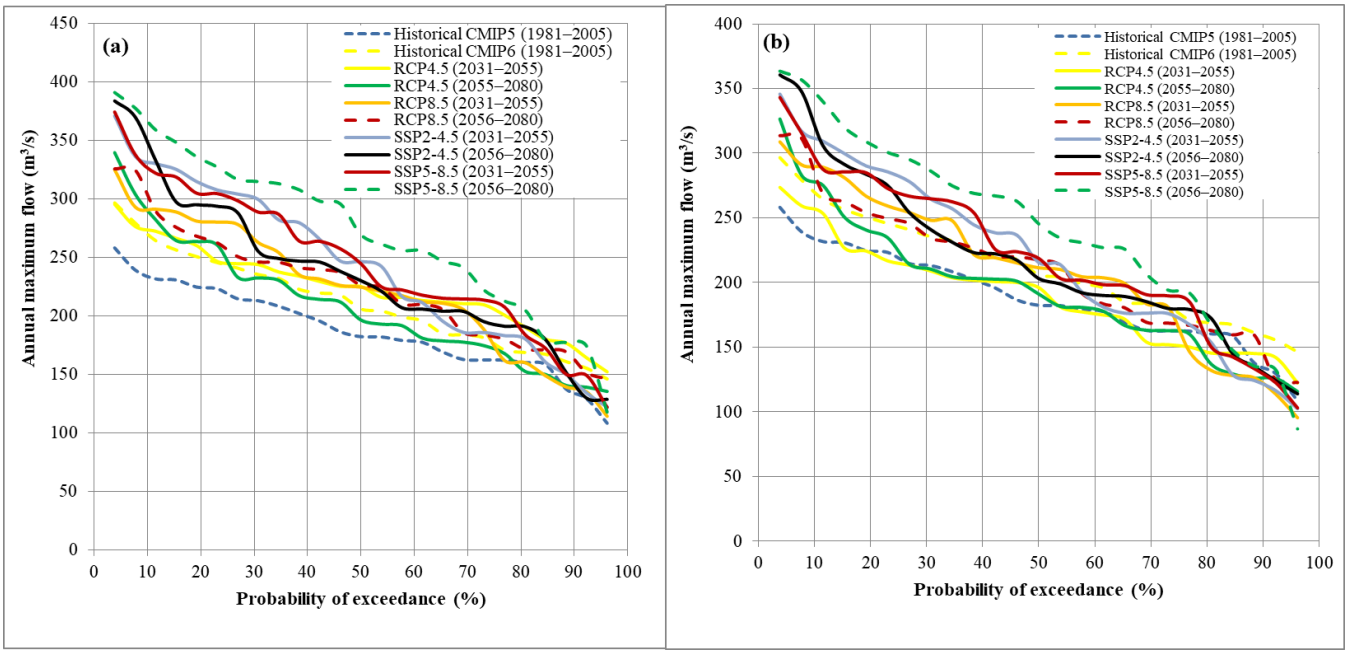

Figure 17. Comparison between historical and future annual maximum 1-day flow duration curves. (**a**) Future climate combined with the BAU land use scenario and (**b**) future climate combined with the GOV land use scenario.

Table 11. The mean annual maximum flow (Q) of the Gumara watershed, in m^3/s, across different probability of exceedance ranges, as estimated under combined climate and land use scenarios.

Scenario/Period	BAU Land Use Scenario	Flow Under Combined Future Climate and BAU Land Use Scenario				GOV Land Use Scenario	Flow Under Combined Future Climate and GOV Land Use Scenario			
		Q_0–Q_{25}	Q_{26}–Q_{50}	Q_{51}–Q_{75}	Q_{76}–Q_{100}		Q_0–Q_{25}	Q_{26}–Q_{50}	Q_{51}–Q_{75}	Q_{76}–Q_{100}
Historical CMIP5 (1981–2005)	_	234.7	200.4	172.3	142.8	_	234.7	200.4	172.3	142.8
Historical CMIP6 (1981–2005)	_	265.5	224.9	191.6	161.7	_	265.5	224.9	191.6	161.7
RCP4.5 (2031–2055)	2035	269.6	234.4	212.9	177.5	2035	242.4	203.5	168.4	141.7
RCP4.5 (2055–2080)	2065	285.7	219.5	182.9	147.8	2065	268.4	203.8	172.1	132.3
RCP8.5 (2031–2055)	2035	293.2	244.6	209.3	143.4	2035	282.7	231	197	123.6
RCP8.5 (2056–2080)	2065	291	241	203.3	165.1	2065	276.7	227.9	184.4	149.3
SSP2-4.5 (2031–2055)	2035	330.8	274.9	206.3	155.2	2035	308	247.8	186	132.1
SSP2-4.5 (2056–2080)	2065	328.7	250.5	206.3	162.1	2065	310.7	227.4	189.2	144.8
SSP5-8.5 (2031–2055)	2035	327	272	218.1	164.3	2035	298.3	245.1	196.9	139.3
SSP5-8.5 (2056–2080)	2065	356.4	302.2	247.2	177.8	2065	331.6	271.5	219.7	143.5

In summary, the use of FDCs provides a robust approach to capture and compare the impacts of different LULC and climate scenarios on high-flow extremes. The increases in high-flow extremes under future scenarios, particularly in the BAU case, emphasize the urgent need for sustainable land use practices and climate adaptation strategies to mitigate future flood risks in the study watershed.

4. Discussion

4.1. Flood Source Area Identification and Analysis of High-Flow Extremes

The downstream part of the Gumara watershed is the most frequently flood-impacted area due to the high runoff contributed by the upstream watershed. This area, which includes cultivated land, rural and urban settlements, and infrastructure, is adversely affected by frequent floods, particularly during the main rainy months of July and August [46,47]. Land use and land cover (LULC) changes, such as deforestation and the expansion of cultivated land, combined with increases in extreme rainfall due to climate change in the upstream watershed, are key factors driving the increased frequency of floods in the region. For these reasons, this study focused on FSAI and the analysis of high-flow extremes under changing LULC and climate conditions in the upstream part of the watershed.

From the FSAI analysis, subwatersheds labeled from W1 to W8 showed varying flood index values under different LULC conditions. Consistent with these findings, a study by Saghafian et al. [113] in the Golestan watershed, located northeast of Iran, and Abdulkareem et al. [39] in the Kelantan River basin, Malaysia, showed the significant contribution of LULC in identifying flood source areas. Overall, for the Gumara watershed, subwatersheds labeled W4 and W6 were identified as the most significant runoff-contributing subwatersheds. This suggests that these two subwatersheds play the largest role in contributing to flooding in the downstream area, making them priority areas for intervention. To mitigate runoff and reduce downstream flooding, it is essential to implement measures in these subwatersheds that enhance infiltration. These measures could include effective land use management strategies (such as afforestation, reforestation, terracing, and contour farming), soil and water conservation practices (e.g., check dams and gabions), and green infrastructure solutions.

The projected high-flow extremes for the future period in this study consistently showed increases relative to the historical period. Notably, the percentage increases were higher when future climate scenarios were combined with the BAU land use scenario. This can be attributed to the fact that, under the BAU scenario, the clearing of forests and other vegetative cover for agricultural expansion leads to decreased infiltration rates and increased surface runoff, resulting in higher flows during extreme rainfall events. These findings are in line with previous studies [115,116], which also projected an increase in streamflow under future climate scenarios combined with the BAU land use scenario. In contrast, when different climate scenarios were combined with the GOV land use scenario, the percentage increases were lower. This is because land use management strategies under the GOV scenario, such as afforestation, reforestation programs, and controlled expansion of cultivated land and settlements, are expected to enhance infiltration and reduce runoff during extreme rainfall events.

Among all simulations of high flows for future periods, the most alarming increase in high flows was observed under the SSP5-8.5 (2056–2080) climate scenario combined with the BAU-2065 land use scenario, consistent with recent studies [42–44]. These results indicate that the Gumara watershed will face more frequent floods during this period, which could significantly disrupt the socioeconomic conditions of the community, as their livelihoods depend on crop cultivation. To reduce the adverse impact of future flood events, this suggests a pressing need to implement various flood protection and adaptation strategies in the downstream part of the watershed. First, it is recommended that local governments implement strict land use management policies that promote afforestation and reforestation to counterbalance the impacts of climate change on flooding. Second, local communities, basin initiatives, and non-governmental organizations should actively participate in soil and water conservation activities. Third, the construction of flood protection infrastructure in the downstream areas, particularly near cultivated land and settlements, is essential

to mitigate the adverse effects of flooding on socioeconomic activities and infrastructure. The feasibility of these flood protection and adaptation measures requires collaboration among local governments, non-governmental organizations, basin initiatives, and the local community.

Overall, this study investigated the impacts of LULC and climate changes on FSAI and high-flow extremes in the Gumara watershed. The identification of flood source areas provides valuable insights for prioritizing subwatersheds that contribute most significantly to peak discharges. This spatially explicit information can guide targeted interventions to mitigate flood risks. By integrating historical and future LULC scenarios with projected climate data, the findings indicate a substantial increase in high-flow extremes in future periods. These increases suggest the likelihood of more frequent flood events, which could adversely impact downstream areas. In this regard, the study provides critical insights into future flood risks and offers a foundation for developing effective flood risk management strategies to mitigate the adverse impacts of frequent flooding in downstream areas. Furthermore, the methodology developed in this study, particularly the application of merged rainfall data from multiple data sources in flood studies, offers a significant contribution to improving hydrological simulations.

4.2. Generalizability of the Study Findings

The Gumara watershed, located in the UBN basin, has unique geographic and socio-economic characteristics. Geographically, it is characterized by steep upstream slopes and flat downstream floodplains. Socioeconomically, the watershed is dominated by rural areas with scattered settlements, where the livelihood is primarily based on a mixed farming system (crop cultivation and livestock raising). While these characteristics make it a valuable case study for assessing the impacts of LULC and climate change, they may limit the generalizability of findings. The results of this study may be most applicable to watersheds with similar socio-economic conditions and geographic settings. Regions with different geographic and socio-economic characteristics, such as urbanized areas or those with advanced flood management infrastructures, may experience varying hydrological responses. However, the study's methodological framework offers a transferable approach that can be adapted to other regions with comparable challenges.

4.3. Limitations of the Study and Future Research Directions

As mentioned in the methods section, historical and future climate scenarios (RCP and SSP) from GCMs are often associated with uncertainties [80,82]. To reduce these uncertainties, it is recommended to correct biases in climate models and use ensembles of multiple models instead of relying on a single model. In this study, bias correction of climate models and the ensemble mean of GCMs were employed to mitigate these uncertainties. Future research could explore various machine learning ensemble prediction (MLEP) approaches to further reduce uncertainties in climate models and use these outputs as inputs to hydrological models.

Both the BAU and GOV LULC scenarios considered in this study rely on assumptions about future socioeconomic and policy developments. However, these assumptions may not fully capture the uncertainties of future land use changes. For instance, the BAU scenario assumes continuity in current land use trends, while the GOV scenario assumes improvement of forest cover. However, sudden policy shifts and regional economic changes could significantly alter the trajectory assumed in these scenarios. In this context, future research could explore the uncertainties associated with these scenarios by considering more intermediate scenarios to further reduce the uncertainties associated with land use projections.

In this study, the antecedent soil moisture was assumed to be at an average condition, as it represents a standard condition for hydrological modeling. Future research could integrate rainfall data with satellite-based soil moisture data to further enhance flood simulations using hydrological models.

Additionally, future research could extend this study by incorporating hydraulic flood modeling for downstream areas of the Gumara watershed. Using the outputs of this study as inputs for detailed hydraulic modeling would enable a more comprehensive analysis of flood inundation and hazard mapping in the region. This approach could provide valuable insights for flood risk management and inform targeted mitigation strategies.

5. Conclusions

This study assessed the impacts of LULC and climate changes on high-flow extremes in the Gumara watershed using the HEC-HMS model. Merged rainfall data (1981–2019) and multi-model ensemble means from CMIP5 and CMIP6 models were utilized for historical (1981–2005), near-future (2031–2055), and far-future (2056–2080) periods, with future climate scenarios projected under RCP4.5, RCP8.5, SSP2-4.5, and SSP5-8.5 pathways. Historical LULC maps (1985, 2000, 2010, and 2019) and projected LULC scenarios (BAU-2035, BAU-2065, GOV-2035, and GOV-2065) were incorporated to analyze the effects of LULC change on flood risk.

The long-term observation period (1981–2019) showed a significant increase in peak discharge under recent LULC conditions, with peak values rising by 24.9% for the 5-year return period and by 17.6% for the 100-year return period, indicating a decreasing influence of LULC changes with higher return periods. The flood source areas identified using the UFR approach revealed subwatersheds W4 and W6 as consistent contributors to high runoff across various LULC conditions, making them priority areas for flood mitigation efforts.

Future projections indicate a further increase in high flows, especially under the SSP5-8.5 (2056–2080) climate scenario combined with BAU-2065 land use, where flows are projected to increase by up to 20.5%, suggesting an increased flood risk in the region. In contrast, the GOV scenario, which promotes afforestation, shows a smaller flow increase of up to 9.0%, demonstrating that sustainable land management practices can help mitigate climate change impacts on extreme flows.

In summary, this study integrated the RF-MERGE, GIS, and HEC-HMS models to investigate the effects of LULC and climate changes on high-flow extremes in the Gumara watershed. The findings provide valuable insights for watershed managers and land use planners to prioritize subwatersheds and develop effective flood risk management practices. The study suggests the coordinated participation of local governments, non-governmental organizations, basin initiatives, and communities to collaboratively mitigate the adverse effects of future flood events. Future research could expand on this work by using climate model ensembles based on MLEP approaches, integrating satellite-based soil moisture data, and conducting hydraulic flood modeling downstream of the Gumara watershed. These efforts would further inform flood mitigation strategies across the region.

Supplementary Materials: The following supporting information can be downloaded at: https://www.mdpi.com/article/10.3390/cli13010007/s1, Figure S1:Inflow hydrographs for different return periods simulated based on LULC-2019; Table S1: Description of Landsat images used for LULC mapping; Table S2: Pettitt test results for the ground-based station; Table S3: Location and elevation information for ground-based rainfall stations located in the Upper Blue Nile basin of Ethiopia used for training during the merging process.

Author Contributions: H.B.: designed the methodology, analyzed the data, interpreted the results, and wrote the manuscript. A.M.M. and G.T.: supervised the study and reviewed, edited, and wrote

the manuscript. H.T.: reviewed, edited, and wrote the manuscript. All authors have read and agreed to the published version of the manuscript.

Funding: This research was financially supported by the Africa Center of Excellence for Water Management (ACEWM), Addis Ababa University, Ethiopia (Project code: 57940-ET).

Data Availability Statement: The data used for this research are available from the first author upon request (email: haile.belay@aau.edu.et).

Acknowledgments: The authors would like to acknowledge the Africa Center of Excellence for Water Management (ACEWM), Addis Ababa University, Ethiopia, for providing financial support for the first author. We acknowledge sources/providers of ground-based rainfall, discharge, and gridded rainfall products, climate models, and elevation and soil data mentioned in Section 2.2 of the manuscript.

Conflicts of Interest: The authors declare no conflicts of interest.

References

1. Shah, A.A.; Ye, J.; Abid, M.; Ullah, R. Determinants of Flood Risk Mitigation Strategies at Household Level: A Case of Khyber Pakhtunkhwa (KP) Province, Pakistan. *Nat. Hazards* **2017**, *88*, 415–430. [CrossRef]
2. Nel, J.L.; Le Maitre, D.C.; Nel, D.C.; Reyers, B.; Archibald, S.; Van Wilgen, B.W.; Forsyth, G.G.; Theron, A.K.; O'Farrell, P.J.; Mwenge Kahinda, J.M.; et al. Natural Hazards in a Changing World: A Case for Ecosystem-Based Management. *PLoS ONE* **2014**, *9*, e95942. [CrossRef] [PubMed]
3. Irannezhad, M.; Minaei, M.; Ahmadian, S.; Chen, D. Impacts of Changes in Climate and Land Cover-Land Use on Flood Characteristics in Gorganrood Watershed (Northeastern Iran) during Recent Decades*. *Geogr. Ann. Ser. A Phys. Geogr.* **2018**, *100*, 340–350. [CrossRef]
4. Mzava, P.; Valimba, P.; Nobert, J. Quantitative Analysis of the Impacts of Climate and Land-Cover Changes on Urban Flood Runoffs: A Case of Dar Es Salaam, Tanzania. *J. Water Clim. Change* **2021**, *12*, 2835–2853. [CrossRef]
5. Kundu, P.M.; Olang, L.O. The Impact of Land Use Change on Runoff and Peak Flood Discharges for the Nyando River in Lake Victoria Drainage Basin, Kenya. *WIT Trans. Ecol. Environ.* **2011**, *153*, 83–94. [CrossRef]
6. Cuo, L. Land Use/Cover Change Impacts on Hydrology in Large River Basins: A Review. In *Terrestrial Water Cycle and Climate Change: Natural and Human-Induced Impacts*; Wiley: Hoboken, NJ, USA, 2016; pp. 103–134, ISBN 9781118971772.
7. Kim, J.B.; Habimana, J.d.D.; Kim, S.H.; Bae, D.H. Assessment of Climate Change Impacts on the Hydroclimatic Response in Burundi Based on Cmip6 Esms. *Sustainability* **2021**, *13*, 12037. [CrossRef]
8. Meresa, H.; Tischbein, B.; Mekonnen, T. *Climate Change Impact on Extreme Precipitation and Peak Flood Magnitude and Frequency: Observations from CMIP6 and Hydrological Models*; Springer: Dordrecht, The Netherlands, 2022; Volume 111, ISBN 0123456789.
9. Yan, R.; Huang, J.; Wang, Y.; Gao, J.; Qi, L. Modeling the Combined Impact of Future Climate and Land Use Changes on Streamflow of Xinjiang Basin, China. *Hydrol. Res.* **2016**, *47*, 356–372. [CrossRef]
10. Taylor, K.E.; Stouffer, R.J.; Meehl, G.A. An Overview of CMIP5 and the Experiment Design. *Bull. Am. Meteorol. Soc.* **2012**, *93*, 485–498. [CrossRef]
11. Almazroui, M.; Saeed, F.; Saeed, S.; Ismail, M.; Ehsan, M.A.; Islam, M.N.; Abid, M.A.; O'Brien, E.; Kamil, S.; Rashid, I.U.; et al. Projected Changes in Climate Extremes Using CMIP6 Simulations Over SREX Regions. *Earth Syst. Environ.* **2021**, *5*, 481–497. [CrossRef]
12. Gebrechorkos, S.; Leyland, J.; Slater, L.; Wortmann, M.; Ashworth, P.J.; Bennett, G.L.; Boothroyd, R.; Cloke, H.; Delorme, P.; Griffith, H.; et al. A High-Resolution Daily Global Dataset of Statistically Downscaled CMIP6 Models for Climate Impact Analyses. *Sci. Data* **2023**, *10*, 611. [CrossRef]
13. Thrasher, B.; Wang, W.; Michaelis, A.; Melton, F.; Lee, T.; Nemani, R. NASA Global Daily Downscaled Projections, CMIP6. *Sci. Data* **2022**, *9*, 262. [CrossRef] [PubMed]
14. Melton, F. *NASA Earth Exchange Global Daily Downscaled Projections (NEX-GDDP)*; NASA: Washington, DC, USA, 2015; pp. 1–8.
15. Jose, D.M.; Dwarakish, G.S. Ranking of Downscaled CMIP5 and CMIP6 GCMs at a Basin Scale: Case Study of a Tropical River Basin on the South West Coast of India. *Arab. J. Geosci.* **2022**, *15*, 120. [CrossRef]
16. Sharma, A.; Kale, G.D. Ranking of General Circulation Models for Surat City by Using a Hybrid Approach. *Water Pract. Technol.* **2022**, *17*, 2186–2198. [CrossRef]
17. Jose, D.M.; Vincent, A.M.; Dwarakish, G.S. Improving Multiple Model Ensemble Predictions of Daily Precipitation and Temperature through Machine Learning Techniques. *Sci. Rep.* **2022**, *12*, 4678. [CrossRef]

18. Raju, K.S.; Kumar, D.N. Review of Approaches for Selection and Ensembling of GCMS. *J. Water Clim. Change* **2020**, *11*, 577–599. [CrossRef]
19. Wang, D.; Liu, J.; Wang, H.; Shao, W.; Mei, C.; Ding, X. Performance Evaluations of CMIP6 and CMIP5 Models for Precipitation Simulation over the Hanjiang River Basin, China. *J. Water Clim. Change* **2022**, *13*, 2089–2106. [CrossRef]
20. Getachew, B.; Manjunatha, B.R. Impacts of Land-Use Change on the Hydrology of Lake Tana Basin, Upper Blue Nile River Basin, Ethiopia. *Glob. Chall.* **2022**, *6*, 2200041. [CrossRef]
21. Miller, J.D.; Hutchins, M. The Impacts of Urbanisation and Climate Change on Urban Flooding and Urban Water Quality: A Review of the Evidence Concerning the United Kingdom. *J. Hydrol. Reg. Stud.* **2017**, *12*, 345–362. [CrossRef]
22. Mewded, M.; Abebe, A.; Tilahun, S.; Agide, Z. Impact of Land Use and Land Cover Change on the Magnitude of Surface Runoff in the Endorheic Hayk Lake Basin, Ethiopia. *SN Appl. Sci.* **2021**, *3*, 742. [CrossRef]
23. Faichia, C.; Tong, Z.; Zhang, J.; Liu, X.; Kazuva, E.; Ullah, K.; Al-Shaibah, B. Using Rs Data-Based ca–Markov Model for Dynamic Simulation of Historical and Future Lucc in Vientiane, Laos. *Sustainability* **2020**, *12*, 8410. [CrossRef]
24. Halmy, M.W.A.; Gessler, P.E.; Hicke, J.A.; Salem, B.B. Land Use/Land Cover Change Detection and Prediction in the North-Western Coastal Desert of Egypt Using Markov-CA. *Appl. Geogr.* **2015**, *63*, 101–112. [CrossRef]
25. Liping, C.; Yujun, S.; Saeed, S. Monitoring and Predicting Land Use and Land Cover Changes Using Remote Sensing and GIS Techniques—A Case Study of a Hilly Area, Jiangle, China. *PLoS ONE* **2018**, *13*, e0200493. [CrossRef] [PubMed]
26. Belay, H.; Melesse, A.M.; Tegegne, G. Scenario-Based Land Use and Land Cover Change Detection and Prediction Using the Cellular Automata–Markov Model in the Gumara Watershed, Upper Blue Nile Basin, Ethiopia. *Land* **2024**, *13*, 396. [CrossRef]
27. Gebresellase, S.H.; Wu, Z.; Xu, H.; Muhammad, W.I. Scenario-Based LULC Dynamics Projection Using the CA–Markov Model on Upper Awash Basin (UAB), Ethiopia. *Sustainability* **2023**, *15*, 1683. [CrossRef]
28. Al Baky, M.A.; Islam, M.; Paul, S. Flood Hazard, Vulnerability and Risk Assessment for Different Land Use Classes Using a Flow Model. *Earth Syst. Environ.* **2020**, *4*, 225–244. [CrossRef]
29. Emam, A.R.; Mishra, B.K.; Kumar, P.; Masago, Y.; Fukushi, K. Impact Assessment of Climate and Land-Use Changes on Flooding Behavior in the Upper Ciliwung River, Jakarta, Indonesia. *Water* **2016**, *8*, 559. [CrossRef]
30. Tegegne, G.; Melesse, A.M.; Asfaw, D.H.; Worqlul, A.W. Flood Frequency Analyses over Different Basin Scales in the Blue Nile River Basin, Ethiopia. *Hydrology* **2020**, *7*, 44. [CrossRef]
31. Hosking, J.R.M.; Wallis, J.R. *Regional Frequency Analysis*; Cambridge University Press: Cambridge, UK, 1997; ISBN 0521430453.
32. Mareuil, A.; Leconte, R.; Brissette, F.; Minville, M. Impacts of Climate Change on the Frequency and Severity of Floods in the Châteauguay River Basin, Canada. *Can. J. Civ. Eng.* **2007**, *34*, 1048–1060. [CrossRef]
33. Yisehak, B. Prediction of Flood Frequency under a Changing Climate, the Case of Hare Watershed, Rift Valley Basin of Ethiopia. *Sustain. Water Resour. Manag.* **2021**, *7*, 9. [CrossRef]
34. Noori, N.; Kalin, L.; Sen, S.; Srivastava, P.; Lebleu, C. Identifying Areas Sensitive to Land Use/Land Cover Change for Downstream Flooding in a Coastal Alabama Watershed. *Reg. Environ. Change* **2016**, *16*, 1833–1845. [CrossRef]
35. Saghafian, B.; Khosroshahi, M. Unit Response Approach for Priority Determination of Flood Source Areas. *J. Hydrol. Eng.* **2005**, *10*, 270–277. [CrossRef]
36. Singh, A.; Dawson, D.; Trigg, M.; Wright, N. A Review of Modelling Methodologies for Flood Source Area (FSA) Identification. *Nat. Hazards* **2021**, *107*, 1047–1068. [CrossRef]
37. Argaz, A.; Ouahman, B.; Darkaoui, A.; Bikhtar, H.; Ayouch, E.; Lazaar, R. Flood Hazard Mapping Using Remote Sensing and GIS Tools: A Case Study of Souss Watershed. *J. Mater. Environ. Sci.* **2019**, *10*, 170–181.
38. Elkhrachy, I. Flash Flood Hazard Mapping Using Satellite Images and GIS Tools: A Case Study of Najran City, Kingdom of Saudi Arabia (KSA). *Egypt. J. Remote Sens. Sp. Sci.* **2015**, *18*, 261–278. [CrossRef]
39. Abdulkareem, J.H.; Sulaiman, W.N.A.; Pradhan, B.; Jamil, N.R. Relationship between Design Floods and Land Use Land Cover (LULC) Changes in a Tropical Complex Catchment. *Arab. J. Geosci.* **2018**, *11*, 376. [CrossRef]
40. Fiorillo, E.; Tarchiani, V. A Simplified Hydrological Method for Flood Risk Assessment at Sub-Basin Level in Niger. In *Renewing Local Planning to Face Climate Change in the Tropics. Green Energy and Technology*; Springer: Cham, Switzerland, 2017; pp. 247–263. [CrossRef]
41. Yang, S.; Yang, D.; Zhao, B.; Ma, T.; Lu, W.; Santisirisomboon, J. Future Changes in High and Low Flows under the Impacts of Climate and Land Use Changes in the Jiulong River Basin of Southeast China. *Atmosphere* **2022**, *13*, 150. [CrossRef]
42. Mahato, P.K.; Singh, D.; Bharati, B.; Gagnon, A.S.; Singh, B.B.; Brema, J. Assessing the Impacts of Human Interventions and Climate Change on Fluvial Flooding Using CMIP6 Data and GIS-Based Hydrologic and Hydraulic Models. *Geocarto Int.* **2022**, *37*, 11483–11508. [CrossRef]
43. Kassaye, S.M.; Tadesse, T.; Tegegne, G.; Hordofa, A.T. Quantifying the Climate Change Impacts on the Magnitude and Timing of Hydrological Extremes in the Baro River Basin, Ethiopia. *Environ. Syst. Res.* **2024**, *13*, 2. [CrossRef]
44. Yalcin, E. Assessing Future Changes in Flood Frequencies under CMIP6 Climate Projections Using SWAT Modeling: A Case Study of Bitlis Creek, Turkey. *J. Water Clim. Change* **2024**, *15*, 2212–2231. [CrossRef]

45. Alemu, D.; Assaye, A. *Devastating Effect of Floods on Rice Production and Commercialisation in the Fogera Plain*; Future Agricultures Consortium Secretariat: Brighton, UK, 2020.
46. Gashaw, W.; Legesse, D. Flood Hazard and Risk Assessment Using GIS and Remote Sensing in Fogera Woreda, Northwest Ethiopia. *Nile River Basin* **2011**, *6*, 179–206. [CrossRef]
47. Nigusie, A.A.; Shiferaw, K.M.; Ebrahim, S.E. Flood Inundation Modeling Using HEC-RAS : The Case of Downstream Gumara River, Lake Tana Sub Basin, Ethiopia. *Geocarto Int.* **2021**, *37*, 9625–9643. [CrossRef]
48. Melkamu, T.; Bagyaraj, M.; Adimaw, M.; Ngusie, A. Detecting and Mapping Flood Inundation Areas in Fogera-Dera Floodplain, Ethiopia during an Extreme Wet Season Using Sentinel-1 Data. *Phys. Chem. Earth Parts A/B/C* **2022**, *127*, 103189. [CrossRef]
49. Molini, A.; Lanza, L.G.; La Barbera, P. The Impact of Tipping-bucket Raingauge Measurement Errors on Design Rainfall for Urban-scale Applications. *Hydrol. Process. Int. J.* **2005**, *19*, 1073–1088. [CrossRef]
50. Belay, H.; Melesse, A.M.; Tegegne, G. Merging Satellite Products and Rain-Gauge Observations to Improve Hydrological Simulation: A Review. *Earth* **2022**, *3*, 1275–1289. [CrossRef]
51. Mekonnen, K.; Melesse, A.M.; Woldesenbet, T.A. Merging Satellite Rainfall Estimates and Daily Rain Gauge Observations for Improved Flood Simulation in MelkaKuntire Catchment, Upper Awash Basin, Ethiopia. *Remote Sens. Appl. Soc. Environ.* **2022**, *25*, 100701. [CrossRef]
52. Baez-Villanueva, O.M.; Zambrano-Bigiarini, M.; Beck, H.E.; McNamara, I.; Ribbe, L.; Nauditt, A.; Birkel, C.; Verbist, K.; Giraldo-Osorio, J.D.; Xuan Thinh, N. RF-MEP: A Novel Random Forest Method for Merging Gridded Precipitation Products and Ground-Based Measurements. *Remote Sens. Environ.* **2020**, *239*, 111606. [CrossRef]
53. Min, X.; Yang, C.; Dong, N. Merging Satellite and Gauge Rainfalls for Flood Forecasting of Two Catchments under Different Climate Conditions. *Water* **2020**, *12*, 802. [CrossRef]
54. Beck, H.E.; Vergopolan, N.; Pan, M.; Levizzani, V.; Van Dijk, A.I.J.M.; Weedon, G.P.; Brocca, L.; Pappenberger, F.; Huffman, G.J.; Wood, E.F. Global-Scale Evaluation of 22 Precipitation Datasets Using Gauge Observations and Hydrological Modeling. *Hydrol. Earth Syst. Sci.* **2017**, *21*, 6201–6217. [CrossRef]
55. Funk, C.; Peterson, P.; Landsfeld, M.; Pedreros, D.; Verdin, J.; Shukla, S.; Husak, G.; Rowland, J.; Harrison, L.; Hoell, A.; et al. The Climate Hazards Infrared Precipitation with Stations—A New Environmental Record for Monitoring Extremes. *Sci. Data* **2015**, *2*, 150066. [CrossRef]
56. Muñoz-Sabater, J.; Dutra, E.; Agustí-Panareda, A.; Albergel, C.; Arduini, G.; Balsamo, G.; Boussetta, S.; Choulga, M.; Harrigan, S.; Hersbach, H.; et al. ERA5-Land: A State-of-the-Art Global Reanalysis Dataset for Land Applications. *Earth Syst. Sci. Data* **2021**, *13*, 4349–4383. [CrossRef]
57. Chakilu, G.G.; Sándor, S.; Zoltán, T. Change in Stream Flow of Gumara Watershed, Upper Blue Nile Basin, Ethiopia under Representative Concentration Pathway Climate Change Scenarios. *Water* **2020**, *12*, 3046. [CrossRef]
58. Wubie, M.A.; Assen, M.; Nicolau, M.D. Patterns, Causes and Consequences of Land Use/Cover Dynamics in the Gumara Watershed of Lake Tana Basin, Northwestern Ethiopia. *Environ. Syst. Res.* **2016**, *5*, 1. [CrossRef]
59. Dawit, M.; Halefom, A.; Teshome, A.; Sisay, E.; Shewayirga, B.; Dananto, M. Changes and Variability of Precipitation and Temperature in the Guna Tana Watershed, Upper Blue Nile Basin, Ethiopia. *Model. Earth Syst. Environ.* **2019**, *5*, 1395–1404. [CrossRef]
60. Ayehu, G.T.; Tadesse, T.; Gessesse, B.; Dinku, T. Validation of New Satellite Rainfall Products over the Upper Blue Nile Basin, Ethiopia. *Atmos. Meas. Tech.* **2018**, *11*, 1921–1936. [CrossRef]
61. Lakew, H.B.; Moges, S.A.; Asfaw, D.H. Hydrological Performance Evaluation of Multiple Satellite Precipitation Products in the Upper Blue Nile Basin, Ethiopia. *J. Hydrol. Reg. Stud.* **2020**, *27*, 100664. [CrossRef]
62. Belay, H.; Melesse, A.M.; Tegegne, G. Evaluation and Comparison of the Performances of the CMIP5 and CMIP6 Models in Reproducing Extreme Rainfall in the Upper Blue Nile Basin of Ethiopia. *Theor. Appl. Climatol.* **2024**, *155*, 9471–9496. [CrossRef]
63. Farr, T.G.; Rosen, P.A.; Caro, E.; Crippen, R.; Duren, R.; Hensley, S.; Kobrick, M.; Paller, M.; Rodriguez, E.; Roth, L. The Shuttle Radar Topography Mission. *Rev. Geophys.* **2007**, *45*, RG2004. [CrossRef]
64. Ross, C.W.; Prihodko, L.; Anchang, J.; Kumar, S.; Ji, W.; Hanan, N.P. HYSOGs250m, Global Gridded Hydrologic Soil Groups for Curve-Number-Based Runoff Modeling. *Sci. Data* **2018**, *5*, 180091. [CrossRef]
65. Breiman, L. Random Forests. *Mach. Learn.* **2001**, *45*, 5–32. [CrossRef]
66. Eastman, J. *IDRISI Taiga: Guide to GIS and Image Processing Volume—Manual Version 16.02*; Clark Labs Clark University: Worcester, MA, USA, 2009; p. 325.
67. Beyene, A.; Shumetie, A. *Green Legacy Initiative for Sustainable Economic Development in Ethiopia*; Ethiopian Economics Association: Addis Ababa, Ethiopia, 2023; ISBN 9789994454952.
68. Déqué, M. Frequency of Precipitation and Temperature Extremes over France in an Anthropogenic Scenario: Model Results and Statistical Correction According to Observed Values. *Glob. Planet. Change* **2007**, *57*, 16–26. [CrossRef]
69. USACE. *Hydrologic Modeling System User' s Manual*; USACE: Washington, DC, USA, 2008; p. 290.
70. Hirsch, R.M. A Comparison of Four Streamflow Record Extension Techniques. *Water Resour. Res.* **1982**, *18*, 1081–1088. [CrossRef]

71. Pettitt, A.N. A Non-Parametric to the Approach Problem. *Appl. Stat.* **1979**, *28*, 126–135. [CrossRef]
72. Breiman, L. *Breiman and Cutler's Random Forests for Classification and Regression*; R Package Version 4.7; University of California, Berkeley: Berkeley, CA, USA, 2018; p. 3.
73. Fan, Z.; Li, W.; Jiang, Q.; Sun, W.; Wen, J.; Gao, J. A Comparative Study of Four Merging Approaches for Regional Precipitation Estimation. *IEEE Access* **2021**, *9*, 33625–33637. [CrossRef]
74. Nguyen, G.V.; Le, X.H.; Van, L.N.; Jung, S.; Yeon, M.; Lee, G. Application of Random Forest Algorithm for Merging Multiple Satellite Precipitation Products across South Korea. *Remote Sens.* **2021**, *13*, 4033. [CrossRef]
75. Anderson, T.W.; Darling, D.A. Asymptotic Theory of Certain "Goodness of Fit" Criteria Based on Stochastic Processes. *Ann. Math. Stat.* **1952**, *23*, 193–212. [CrossRef]
76. Stephens, M.A. EDF Statistics for Goodness of Fit and Some Comparisons. *J. Am. Stat. Assoc.* **1974**, *69*, 730–737. [CrossRef]
77. Bibi, T.S. Derivation of Short-Term Design Rainfall Intensity from Daily Rainfall Data for Urban Drainage Design Using Empirical Equations in Robe Town, Ethiopia. *Int. J. Hydrol.* **2023**, *7*, 63–71. [CrossRef]
78. Zinabie, A.; Kebede, B. Hydraulic Analysis of Storm Water Drainage System in Alamata Town, South Tigray, Ethiopia. *Iran. J. Energy Environ.* **2020**, *11*, 40–50. [CrossRef]
79. Acharya, N.; Chattopadhyay, S.; Mohanty, U.C.; Dash, S.K.; Sahoo, L.N. On the Bias Correction of General Circulation Model Output for Indian Summer Monsoon. *Meteorol. Appl.* **2013**, *20*, 349–356. [CrossRef]
80. Kaur, K.; Kaur, N. Comparison of Bias Correction Methods for Climate Change Projections in the Lower Shivaliks of Punjab. *J. Water Clim. Change* **2023**, *14*, 2606–2625. [CrossRef]
81. Yamamoto, K.; Sayama, T. Apip Impact of Climate Change on Flood Inundation in a Tropical River Basin in Indonesia. *Prog. Earth Planet. Sci.* **2021**, *8*, 5. [CrossRef]
82. Enayati, M.; Bozorg-Haddad, O.; Bazrafshan, J.; Hejabi, S.; Chu, X. Bias Correction Capabilities of Quantile Mapping Methods for Rainfall and Temperature Variables. *J. Water Clim. Change* **2021**, *12*, 401–419. [CrossRef]
83. Soriano, E.; Mediero, L.; Garijo, C. Selection of Bias Correction Methods to Assess the Impact of Climate Change on Flood Frequency Curves. *Water* **2019**, *11*, 2266. [CrossRef]
84. Ghonchepour, D.; Sadoddin, A.; Bahremand, A.; Croke, B.; Jakeman, A.; Salmanmahiny, A. A Methodological Framework for the Hydrological Model Selection Process in Water Resource Management Projects. *Nat. Resour. Model.* **2021**, *34*, e12326. [CrossRef]
85. Acharya, A.; Lamb, K.; Piechota, T.C. Impacts of Climate Change on Extreme Precipitation Events Over Flamingo Tropicana Watershed. *J. Am. Water Resour. Assoc.* **2013**, *49*, 359–370. [CrossRef]
86. Tibangayuka, N.; Mulungu, D.M.M.; Izdori, F. Assessing the Potential Impacts of Climate Change on Streamflow in the Data-Scarce Upper Ruvu River Watershed, Tanzania. *J. Water Clim. Change* **2022**, *13*, 3496–3513. [CrossRef]
87. Sanyal, J.; Densmore, A.L.; Carbonneau, P. Analysing the Effect of Land-Use/Cover Changes at Sub-Catchment Levels on Downstream Flood Peaks: A Semi-Distributed Modelling Approach with Sparse Data. *Catena* **2014**, *118*, 28–40. [CrossRef]
88. Jemberie, M.A.; Awass, A.A.; Melesse, A.M.; Ayele, G.T.; Demissie, S.S. Seasonal Rainfall–Runoff Variability Analysis, Lake Tana Sub-Basin, Upper Blue Nile Basin, Ethiopia. In *Landscape Dynamics, Soils and Hydrological Processes in Varied Climates*; Springer: Cham, Switzerland, 2016; pp. 341–363.
89. Tassew, B.G.; Belete, M.A.; Miegel, K. Application of HEC-HMS Model for Flow Simulation in the Lake Tana Basin: The Case of Gilgel Abay Catchment, Upper Blue Nile Basin, Ethiopia. *Hydrology* **2019**, *6*, 21. [CrossRef]
90. Cronshey, R. *Urban Hydrology for Small Watersheds*; US Department of Agriculture, Soil Conservation Service, Engineering Division: Washington, DC, USA, 1986.
91. Cunge, J.A. On the Subject of a Flood Propagation Computation Method (Musklngum Method). *J. Hydraul. Res.* **1969**, *7*, 205–230. [CrossRef]
92. Redlands, C. *ArcGIS Desktop: Release 10*; Environmental Systems Research Institute: Redlands, CA, USA, 2011.
93. Kirpich, Z.P. Time of Concentration of Small Agricultural Watersheds. *Civ. Eng.* **1940**, *10*, 362.
94. Chow, V.T.; Maidment, D.R.; Mays, L.W. *Applied Hydrology*; McGraw-Hill: NewYork, NY, USA, 1988; ISBN 0070108102.
95. Song, X.; Zhang, J.; Zhan, C.; Xuan, Y.; Ye, M.; Xu, C. Global Sensitivity Analysis in Hydrological Modeling: Review of Concepts, Methods, Theoretical Framework, and Applications. *J. Hydrol.* **2015**, *523*, 739–757. [CrossRef]
96. Legates, D.R.; McCabe Jr, G.J. Evaluating the Use of "Goodness-of-fit" Measures in Hydrologic and Hydroclimatic Model Validation. *Water Resour. Res.* **1999**, *35*, 233–241. [CrossRef]
97. Van Liew, M.W.; Veith, T.L.; Bosch, D.D.; Arnold, J.G. Suitability of SWAT for the Conservation Effects Assessment Project: Comparison on USDA Agricultural Research Service Watersheds. *J. Hydrol. Eng.* **2007**, *12*, 173–189. [CrossRef]
98. Nash, J.E.; Sutcliffe, J. V River Flow Forecasting through Conceptual Models Part I—A Discussion of Principles. *J. Hydrol.* **1970**, *10*, 282–290. [CrossRef]
99. Gupta, H.V.; Sorooshian, S.; Yapo, P.O. Status of Automatic Calibration for Hydrologic Models: Comparison with Multilevel Expert Calibration. *J. Hydrol. Eng.* **1999**, *4*, 135–143. [CrossRef]

100. Moriasi, D.N.; Arnold, J.G.; Van Liew, M.W.; Bingner, R.L.; Harmel, R.D.; Veith, T.L. Model Evaluation Guidelines for Systematic Quantification of Accuracy in Watershed Simulations. *Trans. ASABE* **2007**, *50*, 885–900. [CrossRef]
101. Alaminie, A.A.; Tilahun, S.A.; Legesse, S.A.; Zimale, F.A.; Tarkegn, G.B.; Jury, M.R. Evaluation of Past and Future Climate Trends under CMIP6 Scenarios for the UBNB (Abay), Ethiopia. *Water* **2021**, *13*, 2110. [CrossRef]
102. Ayalew, D.W.; Asefa, T.; Moges, M.A.; Leyew, S.M. Evaluating the Potential Impact of Climate Change on the Hydrology of Ribb Catchment, Lake Tana Basin, Ethiopia. *J. Water Clim. Change* **2022**, *13*, 190–205. [CrossRef]
103. Chakilu, G.G.; Sándor, S.; Zoltán, T. The Dynamics of Hydrological Extremes under the Highest Emission Climate Change Scenario in the Headwater Catchments of the Upper Blue Nile Basin, Ethiopia. *Water* **2023**, *15*, 358. [CrossRef]
104. Fischer, T.; Su, B.; Luo, Y.; Scholten, T. Probability Distribution of Precipitation Extremes for Weather Index-Based Insurance in the Zhujiang River Basin, South China. *J. Hydrometeorol.* **2012**, *13*, 1023–1037. [CrossRef]
105. Benyahya, L.; Gachon, P.; St-Hilaire, A.; Laprise, R. Frequency Analysis of Seasonal Extreme Precipitation in Southern Quebec (Canada): An Evaluation of Regional Climate Model Simulation with Respect to Two Gridded Datasets. *Hydrol. Res.* **2014**, *45*, 115–133. [CrossRef]
106. Anteneh, M.; Mohammed, W. Effects of Land Cover Changes and Slope Gradient on Soil Quality in the Gumara Watershed, Lake Tana Basin of North—West Ethiopia. *Model. Earth Syst. Environ.* **2020**, *6*, 85–97. [CrossRef]
107. Chakilu, G.G.; Moges, M.A. Assessing the Land Use/Cover Dynamics and Its Impact on the Low Flow of Gumara Watershed, Upper Blue Nile Basin, Ethiopia. *Hydrol. Curr. Res.* **2017**, *8*, 1–6. [CrossRef]
108. Zelelew, D.G.; Melesse, A.M. Applicability of a Spatially Semi-Distributed Hydrological Model for Watershed Scale Runoff Estimation in Northwest Ethiopia. *Water* **2018**, *10*, 923. [CrossRef]
109. Yilma, Z.L.; Kebede, H.H. Simulation of the Rainfall-Runoff Relationship Using an HEC-HMS Hydrological Model for Dabus Subbasin, Blue Nile Basin, Ethiopia. *H2Open J.* **2023**, *6*, 331–342. [CrossRef]
110. USACE. *Hydrologic Modeling System HEC-HMS Technical Reference Manual*; Hydrologic Engineering Center: Davis, CA, USA, 2000; p. 158.
111. OCHA. *Eastern Africa Region (Regional Floods Snapshot)*; OCHA: Geneva, Switzerland, 2019; p. 2019.
112. Chen, Y.; Xu, Y.; Yin, Y. Impacts of Land Use Change Scenarios on Storm-Runoff Generation in Xitiaoxi Basin, China. *Quat. Int.* **2009**, *208*, 121–128. [CrossRef]
113. Saghafian, B.; Farazjoo, H.; Bozorgy, B.; Yazdandoost, F. Flood Intensification Due to Changes in Land Use. *Water Resour. Manag.* **2008**, *22*, 1051–1067. [CrossRef]
114. Maghsood, F.F.; Moradi, H.; Bavani, A.R.M.; Panahi, M.; Berndtsson, R.; Hashemi, H. Climate Change Impact on Flood Frequency and Source Area in Northern Iran under CMIP5 Scenarios. *Water* **2019**, *11*, 273. [CrossRef]
115. Mengistu, A.G.; Woldesenbet, T.A.; Dile, Y.T.; Bayabil, H.K.; Tefera, G.W. Modeling Impacts of Projected Land Use and Climate Changes on the Water Balance in the Baro Basin, Ethiopia. *Heliyon* **2023**, *9*, e13965. [CrossRef]
116. Teklay, A.; Dile, Y.T.; Asfaw, D.H.; Bayabil, H.K.; Sisay, K. Impacts of Climate and Land Use Change on Hydrological Response in Gumara Watershed, Ethiopia. *Ecohydrol. Hydrobiol.* **2021**, *21*, 315–332. [CrossRef]

Disclaimer/Publisher's Note: The statements, opinions and data contained in all publications are solely those of the individual author(s) and contributor(s) and not of MDPI and/or the editor(s). MDPI and/or the editor(s) disclaim responsibility for any injury to people or property resulting from any ideas, methods, instructions or products referred to in the content.